Master Thesis

Examination of Drivers of Large Surface Melt on the Greenland Ice Sheet

Jeremy Trotereau

TU Delft

Examination of Drivers of Extreme Surface Melt on the Greenland Ice Sheet

Master Thesis

Jeremy Trotereau

Supervision:

Miren Vizcaíno
Michiel van den Broeke
Stef Lhermitte
Marc Schleiss

A thesis presented for the degree of
Master of Civil Engineering

Geoscience and Remote Sensing
Delft University of Technology
The Netherlands

Abstract

The Greenland Ice Sheet (GrIS) is an ice sheet situated on the island of Greenland. It has a surface area of about 1.74 million km² and contains a volume of ice equivalent to 7.4 m of global mean sea level rise. The GrIS is vulnerable to climate disruptions such as anthropogenic climate change. As a result of increased greenhouse gas emissions, the mass of the GrIS is observed to be decreasing starting in the 1990.

Our research uses output from a climate model called Community Earth System Model version 2.1 (CESM2.1). CESM is an earth system model, meaning that it tries to model the whole earth for its major physical, chemical and biological functions. Importantly for our research, it models the GrIS such that its shape can change, so that it can model changes in atmospheric flow. This is known as an "interactive ice sheet". This research three scenarios run on an interactive ice sheet to find its results. It uses a historical run to evaluate the model. Then it also uses two hypothetical scenarios called 3xCO2 and 4xCO2. Each starts at the pre-industrial concentration of 285 ppm CO2, and then increases the concentration by 1This thesis focuses on the mass balance (MB) of the GrIS, as these differ strongly between 3xCO2 and 4xCO2. In the scenarios we researched, this mass balance is dominated by the surface mass balance (SMB). SMB is in turn primarily driven by the ice melt. Negative SMB is called Ablation Area SMB The thesis makes two important observations. Firstly, area distribution can be split up into a total surface area component, which depends on time, and a relative elevation distribution component, which depends on elevation. Secondly, the area normalised AASMB is linear with elevation, but the gradient varies with time. Typically, increased melt is explained as a result of ablation area expansion. However, this does not capture the elevation distribution of the AASMB. Using the two results drawn from above, we create a new mental model which results in a more detailed explanation of the GrIS mass loss.

Abbreviations

$3xCO_2$	A climate forcing scenario (see figure 2.2)
$4xCO_2$	A climate forcing scenario (see figure 2.2)
AA	Ablation Area
AASMB	SMB in the Ablation Area
AWS	Automatic Weather Station
BMB	Basal Mass Balance
CAM	Community Atmosphere Model
CCM	Community Climate Model
CESM	Community Earth System Model
CISM	Community Ice Sheet Model
CLM	Community Land Model
CMIP6	Coupled Model Intercomparison Project Phase 6
ELA	Equilibrium Line Altitude
ESM	Earth System Model
GCM	Global Climate Model
GHF	Ground Heat Flux
GrIS	Greenland Ice Sheet
ID	Ice Discharge
JJA	June July August
LHF	Latent Heat Flux
LWnet	Net long-wave radiation
LWR	Long-wave radiation
LWU	Upward long-wave radiation
MB	Mass Balance
NCAR	National Center for Atmospheric Research
PI	A pre-industrial climate forcing scenario
RCP	Representative Concentration Pathway
SEB	Surface Energy Balance
SHF	Sensible Heat Flux
SLR	Sea Level Rise
SMB	Surface Mass Balance
SW	Short-wave or South-West
SWnet	Net short-wave radiation
SWR	Short-wave radiation
SWU	Upward short-wave radiation

Acknowledgements

A thesis is not something you do alone. All along the way people gave encouragement and wisdom with their words and actions. I cannot do justice to them all. But the most important are as follows.

Stef, Marc and Michiel enriched my work with their insights, and tough questions. Miren stuck with me every week for a year, adding rigour and method to my work. Noa tempered the bad and brightened the good. Marion brought structure and discipline when I needed it the most. My family had endless patience and compassion. My friends listened and agreed.

Jeremy Trotereau
May 2023

Contents

1

Introduction

1.1. The Greenland Ice Sheet

Situated on the island of Greenland, the Greenland Ice Sheet (GrIS) is a large expanse of ice (about 1.74 million km^2), which covers most, but not all of the area on the Greenland island (Wang et al., 2017). The ice sheet contains the equivalent of 7,4 m of sea level rise (SLR) (Bamber et al., 2013), meaning that its melt significant has a significant impact on global sea levels. The GrIS is considered one of the major tipping elements in the earth system (Lenton et al., 2008). This means that a small perturbation on the GrIS has large and lasting effects on the earth climate system.

As of 2014, the GrIS contributed about 25% all mass increase to the world's oceans (Chen et al., 2017). Of this, the majority is contributed by a relatively small ablation area, which represents only 22% of the GrIS area (Box et al., 2012; Ryan et al., 2019).

The Greenland Ice Sheet has been the subject of extensive scientific research. Despite this, much remains to be learned about GrIS mass loss. For instance, the speed of current surface mass current mass loss was underestimated by model predictions (Slater et al., 2020).

1.1.1. History of the GrIS

The island of Greenland has a long history of glaciation. Paleoclimatic records from before about 16 Ma (million years ago) are scarce, but Alley et al., 2010 conclude that "Despite lack of conclusive evidence, Greenland seems to have supported at least some glaciation since at least 38 Ma". They also note that sea-bed deposits indicating glacial activity increase both at both 14 Ma and 3 Ma.

That last number, 3 million years ago, is generally accepted from observations and simulations to be the start of the main glaciation that saw the island of Greenland obtain an ice sheet (Lunt et al., 2008; Maslin et al., 1998). We know that from there, the GrIS has changed size in response to climate, becoming significantly larger during ice ages and smaller during warm interglacial periods. And finally, we know that it had a significant effect on the cooling of the remainder of the earth system (Maslin et al., 1998).

More recently, starting in the late 1990s, the GrIS started experiencing enhanced melt. This caused increased scientific interest into the GrIS. Notable melt episodes took place in 2010 and 2012. These years saw unusually high summer temperatures, which resulted in a record breaking melt area (Nghiem et al., 2012; Scambos et al., 2013). The decrease in mass balance observed in the 1990s stems primarily from ice discharge. Decreases in SMB followed in the 2000s, which then quickly became the major cause of mass loss (Mouginot et al., 2019).

Between 2006 and 2018 the current enhanced mass loss rate was 0.63 mm of global mean sea level equivalent per year, or 227.9 Gt (gigatonnes) per year. The main causes of mass loss are from surface melt and iceberg calving, with smaller contributions from sublimation and basal melting (Fox-Kemper et al., 2021).

1.2. Mass balance

Mass change of the Greenland Ice Sheet is can be captured using the following formula

$$\text{MB} = \text{BMB} + \text{SMB} - \text{ID} \tag{1.1}$$

Where MB is the total Mass Balance over the whole ice sheet. The BMB is the Basal Mass Balance, the mass loss at the base of the ice sheet, which is driven by geothermal heat flux and frictional heat from flow. BMB is therefore positive for the GrIS. The SMB is the Surface Mass Balance at the top of the ice sheet. It is composed of mass contributors that will be outlined in equation 1.2. And finally the ID is the Ice Discharge, which is the loss of ice to calving at the edge of the ice sheets through outlet glaciers. Of course, the loss of ice to icebergs is not reversible, and therefore the ice discharge is positive or zero, meaning that it is always a mass loss in the mass balance.

The SMB can be subdivided into four components as shown in equation 1.2.

$$\text{SMB} = \text{snowfall} + \text{refreezing} - \text{melt} - \text{sublimation} \tag{1.2}$$

Snowfall represents the increase of the ice sheet due to frozen precipitation. Snow is a porous material, and if the snow is cold enough, these pores can be filled by freezing liquid water in them.

Refreezing depends on three factors: the availability of liquid water, the availability of pores, and the snow layer temperature being sufficiently low to refreeze the water. The available liquid water can come from two different sources: rainwater that is frozen and melt-water that is refrozen. This means that refreezing can partially compensate melt, but can also change water that was never frozen into a mass increase in the ice sheet. The availability of pore space is usually not a restriction, with the exception of high melt scenarios, or exposure of bare ice, as pure ice has no pore space and therefore no refreezing capacity. The layer temperature depends on the climate. In sufficiently cold scenarios, all liquid water can be refrozen. By contrast, in situations of higher melt, the temperature of the snowpack will increase until it can no longer support any refreezing.

The melt term includes all transitions of water from the solid to liquid state. The energy available to melt is dictated by the Surface Energy Balance (SEB), which can be seen in equation 1.3.

The sublimation flux describes all transitions of water from the solid to the gaseous phase. The energy available to sublimation is also a term in the SEB (equation 1.3), namely the latent heat flux (LHF). Of all four fluxes, sublimation is the only one to be able to be negative, which would mean that it adds mass to the GrIS.

The surface energy balance can be written as:

$$\text{SEB} = \text{SW}_{\text{net}} + \text{LW}_{\text{net}} + \text{SHF} + \text{LHF} + \text{GHF} \tag{1.3}$$

The net shortwave radiation is the difference between incoming and outgoing solar radiation, which is always positive. This term can also be rewritten as: $\text{SW}_{\text{net}} = (1-\alpha)SW_{down}$, where α is the albedo, which is a value smaller than one. Examples of albedo values are:

Material	Albedo
Pure fresh snow	0.9
Pure old snow	0.8
Dirty fresh snow	0.7
Dirty old snow	0.4
Bare ice	0.4

Table 1.1: Albedo values for snow and ice, from Willeit and Ganopolski, 2018 and Gardner and Sharp, 2010, respectively

The net longwave radiation is the difference between downward incoming and outgoing longwave radiation. The main difference between longwave radiation and shortwave is that the earth emits longwave radiation, whereas it reflects short wave radiation. Net longwave can be both positive and negative. Positive net longwave indicates a warming of the ice sheet, negative values indicate a cooling.

The Sensible Heat Flux (SHF) is the energy exchanged with the atmosphere as warmth. For example, if the atmosphere is warm and the ice sheet is cool, the SHF is positive as it warms the ice sheet. The SHF can both heat and cool the ice sheet.

The Latent Heat Flux (LHF) is the energy exchanged with the atmosphere in the form of phase. On an ice sheet where, by definition, the surface is frozen, the LHF is the energetic impact of the sublimation flux discussed above (equation 1.2).

Finally, the Ground Heat Flux (GHF) is energy conducted to the ice sheet surface from layers below. It can both heat and cool the ice sheet surface. It is relatively small, and will therefore not be discussed in this thesis.

1.3. State of the art and research gap

Slater et al., 2021 show that current global climate models (GCM) currently struggle to capture contemporary melt variability between high melt years such as 2012 (Scambos et al., 2013) and lower melt periods thereafter (Williams et al., 2020).

The record melt episode in 2012 has been extensively researched. The extent of the melt area was unprecedented in the satellite records, reaching over 98% of the GrIS area (Nghiem et al., 2012; Scambos et al., 2013). It coincided an atmospheric high pressure "blocking" system that created warm southerly winds in West Greenland, causing record breaking air temperatures the area. These in turn caused the extreme melt (Hanna et al., 2014) Refreezing during the melt episode created new ice layers within the firn layer on the GrIS (Nilsson et al., 2015).

The meteorological circumstances that enabled the 2012 melt event are predicted to increase in frequency (see table 9 Hanna et al., 2014) such that by 2100, the probability of similar atmospheric conditions is 52% per year in a moderate (RCP4.5) climate scenario, and 99% per year for an extreme (RCP8.5) climate scenario. Hence the need to study not just the individual extreme melt episodes, but also their cumulative effect on the ice sheet.

Hanna et al., 2014 points out in its conclusion that global climate models (GCMs) struggle to reproduce the kinds of atmospheric conditions that led to the extreme melt episode in 2012. Therefore, our research will focus on melt episodes as a result of extreme forcing rather contemporary forcing.

This leads us to the 3xCO_2 and 4xCO_2 scenarios. These are an extreme, and a very extreme scenario respectively. The scenarios are very simple, consisting of a transitive period, where the CO_2 concentration increases by 1% per year, followed by a CO_2 concentration plateau at 855 and 1140 ppmv CO_2 respectively. This 3 and 4 times the pre-industrial initial 285 ppmv concentration. The 1140 ppmv plateau value is similar to the CO_2 concentration for RCP8.5 (Meinshausen et al., 2020). The rapid increase simulates the rapid change in mass balance observed starting in the 1990s. The concentration plateau aides analysis, while using two different plateaus enables a discussion about the sensitivity of extreme melt for CO_2 concentration.

When discussing repeated extreme mass loss episodes, this eventually has an impact on the thickness of the ice pack, and therefore on the elevation of the ice sheet. Current mass loss to surface melt is about 0.5 m annually in the ablation area according to Slater et al., 2021. Future extreme melt episodes will cause larger melt rates, and therefore impact the elevation and extent of the ice sheet. This work will be focusing on the feedback represented by the elevation dependant variables SMB and hypsometry have on GrIS surface mass loss, and therefore elevation.

In order to place the extreme mass loss on the GrIS into a global perspective, we will have to turn to a specific type of GCM: The Earth System Model. ESMs model climate, but in contrast to global climate models are also able to quantify the response of biogeochemical processes (such as the nitrogen cycle, for instance) to climate change. They are the most complex planet-wide models that exist.

The inclusion of land ice in ESMs is a recent feature (see figure 2, Zhou et al., 2022) which is still yet to reach its full potential. For CESM2, the limitations include simplistic ice calving dynamics, an absence of cross-referencing with the ocean model, and a poor modelling of surface melt ponds, and poor inter-model agreement on initial historical topography. (Goelzer et al., 2020; Muntjewerf et al., 2021). Despite these shortcomings, ESMs have been essential to the future climate. Notable uses include research thresholds for GrIS deglaciation (e.g. Ridley et al., 2009) and committed melt (Noël et al., 2021).

GCMs that allow the ice sheet to grow and shrink are called coupled climate and ice sheet models, and are both novel and rare (Madsen et al., 2022), and would benefit much from improvements (de Boer et al., 2017). However, they have proven valuable tools in the analysis of the GrIS. One Earth System Model including an interactive Greenland ice sheet is the Community Earth System Model, or CESM (used in, Muntjewerf, Sellevold, et al., 2020; Muntjewerf, Petrini, et al., 2020).

1.4. Modelling the GrIS with the CESM

In 1984, the U.S.'s National Center for Atmospheric Research (NCAR) released the first version of the Community Climate Model (CCM), the predecessor of the Community Earth System Model (CESM) used in this master thesis. The CCM modelled the global atmosphere. In 1998, CCM was expanded with components for land, ocean and sea ice (Dickinson et al., 2000). Fluxes of mass, energy and momentum between these four components are exchanged through a coupler, that regulates the frequency of coupling and interpolates between different model components grids (see figure 1, CESM, 2020; Danabasoglu et al., 2020).

The component simulating ice sheet thermomechanics is called the Community Ice Sheet Model (CISM). It is a successor to an ice sheet model called Glimmer (Rutt et al., 2009). The main difference between the two is that Glimmer uses the more simplistic shallow ice approximation to calculate ice velocities, whilst CISM2.1 utilises the Blatter-Pattyn approximation (Lipscomb et al., 2019).

What makes CESM2.1-CISM2.1 a coupled ice-sheet and climate model is that CISM interacts with CLM to ajust the height of the GrIS every 5 years, and that CLM and CAM interact to ensure that elevation gradients are applied. The ocean component only has a one-way interaction, as it recieves meltwater and ice discharge from the GrIS, but does not influence the marine-terminating glaciers on the GrIS directly. CISM is developed specially to run with CESM2.0 input (Lipscomb et al., 2019; Muntjewerf, Sellevold, et al., 2020).

The model artificially splits the GrIS into two layers. The ice in the GrIS falls under CISM, whereas any snow or firn cover lies within the purview of Community Land Model (CLM), the land component. To save computational power, ESMs such as CESM will vary their resolution across components. We note above that the land component (CLM) has a lower spatial resolution of about 1 degree. It has a temporal resolution of 3 hours. The ice sheet component (CISM) has a much higher spatial resolution of about 4km, but has a temporal resolution of 1 year.

As a result of its relatively high resolution in both the climate and ice sheet components and complexity, CESM pushes the boundaries of available computational power. This results in a trade-off between complexity, and spatial and temporal resolution (Flato, 2011). This means that models such as CESM cannot be used for analyses that require high resolution or long time series.

ESMs with coupled ice sheet are still a novelty. They enable the analysis of the sensitivity of the GrIS to mass loss (Vizcaino, 2014), and how changes in elevation impact the surface mass balance, Vizcaino et al., 2015, e.g.

The model runs we will use have been partly analysed by Muntjewerf, Petrini, et al., 2020. That paper, finds that mass loss increases over time for a 350-year-long 1% to 4xCO2 scenario (also when the CO_2 concentration is held constant), and that ablation zones in the GrIS expand substantially in connection with the pseudo-parabolic elevation distribution of area of the ice sheet. In an unpublished figure (figure 1.1), we see different runs by CESM2.1. We see that there are large changes in mass loss rates between the $3xCO_2$ and $4xCO_2$ scenarios. By year 500, mass loss rates are about 1000 Gt/yr for $3xCO_2$ and 3000 Gt/yr for $4xCO_2$.

As mentioned in section 1.3, we are interested in severe mass loss. Between extreme ($3xCO_2$) and very extreme ($4xCO_2$) GHG forcing, we observe significantly different melt rates. We will explore the mechanisms explaining these differences.

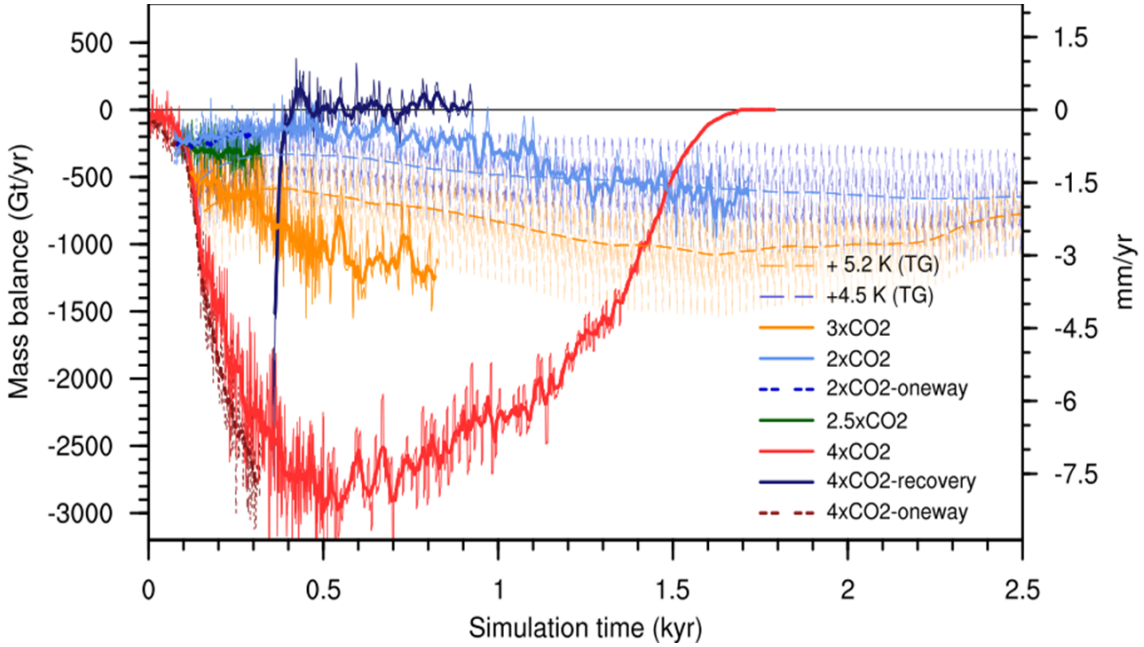

Figure 1.1: Contribution to sea level rise (right y-axis, in Gt/yr; left y-axis, in mm sea level rise per year) for different scenarios run with the CESM2.1-CISM2.1 (unpublished, by Michele Petrini). The runs are fully coupled except for the "oneway" and "TG" runs. The 5.2 and 4.5 K "TG" runs indicate CISM-only runs that use repeated offline elevation-dependent SMB climatological forcing corresponding to those global warming levels from the transient 4xCO_2 simulation. All other runs start from an initial pre-industrial CO_2 concentration, and increase that with 1% per year until it is the indicated factor larger (be that 2, 2.5, 3 or 4 times). "Recovery" means that the CO_2 concentration is reduced from 4xCO2 to pre-industrial over a period of 20 years.)

1.5. Research questions

As noted in section 1.3, we do not yet have a clear understanding of the impacts of successive melt events on the GrIS. In order to gauge this impact, we analyse two extreme mass loss scenarios as proxies for successive melt events. Hence our main research question is:

How would future GrIS mass loss rates respond to extreme and very extreme forcing?

To analyse this, we will used two idealised CO_2 scenarios. The are the 3xCO_2 and 4xCO_2 scenarios, which both increase CO_2 concentrations with 1 % per year until reaching three and four times initial concentration respectively. The advantages of these models is that it is relatively easy to attribute behaviour to transient or static CO_2 concentrations. Another advantage is that both scenarios are very similar in design, (indeed they have a common start).

We will split the research question up into three parts. Each is connected to one question

1. How well do the elevation profiles of GrIS SMB and SEB components match observations on the GrIS?

This question aims to evaluate the robustness of the projections from the model. The argumentation of this thesis relies to a large extent on an accurate model representation of elevation gradients of SMB, and to a lesser extent SEB. To evaluate these, we use direct observations from the K-transect, a series of automatic weather stations (AWS) situated in the West of Greenland at about 67° N. Though this gives only a local evaluation, the K-transect has two advantages. Firstly, it is located on a shallow slope, meaning that the elevation gradient can be resolved by the model (as opposed to very steep location, such as SW Greenland). Furthermore, the K-transect is situated in South-West Greenland, which is a climatically sensitive region, as it is the largest contributor within the GrIS to surface runoff (see figure 2 Noël et al., 2019) and likely to deglaciate even under moderate warming by 3000 (Aschwanden et al., 2019).

2. Which mass-loss related variables differ significantly between a high (3xCO2) and a very high (4xCO2) scenario?

This will be done using tables, maps, timeseries and transects. The tables give a good indication of absolute values, the maps of spatial patterns, the timeseries of temporal patterns. The transects give an idea of the influence of elevation and local climate.

3. How does local SMB vary with elevation and how does that influence GrIS surface mass loss?

To answer this question, we will discuss the change in hypsometry over time. We create a simple mental model based on linear SMB in the ablation area and combine it with a stable hypsometry to find that three variables influence the total surface mass loss.

2

Methods

2.1. Model description

As already noted in the introduction, CESM2 is subdivided into multiple components that are connected by a coupler. A schematic overview of these model components and how they interact can be seen in figure 2.1. from these, we will describe the three components that are most important in modelling the ice sheet. CLM5, which models snow cover on the ice sheet, CISM2, which models the ice sheet, and CAM6, which models atmospheric conditions above the ice sheet.

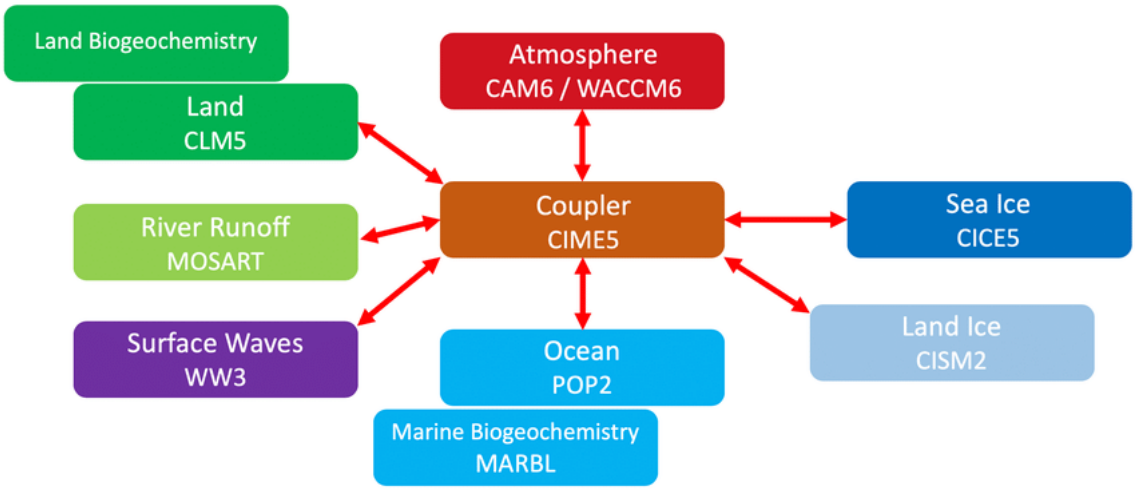

Figure 2.1: CESM2 model components and interactions from Danabasoglu et al., 2020

2.1.1. CLM5

The first model component that is relevant to calculate GrIS evolution is the Community Land Model, CLM5. CLM runs the relevant physical and chemical processes on the land surface as well as the subsurface. As well as the snow/firn layer on the GrIS. It does this primarily on an approximately 1° grid.

Given the heterogeneity that can occur within a 1° grid cell, the cell is subdivided into five different landunits. These are: Soil, lake, urban, glacier and crop. The GrIS falls under glaciers, which CLM subdivides into 10 elevation classes (lower limit are 0, 200, 400, 700, 1000, 1300, 1600, 2000, 2500, and 3000 m), and then calculates atmospheric forcing at each elevation (CESM, 2020; Sellevold et al., 2019).

The atmospheric forcing from CAM is recalculated for each elevation class using prescribed lapse rates. In the CESM2-CISM2 simulations analysed in this thesis, relative humidity is kept constant over the elevations, as is the downwelling longwave radiation. On the contrary, the temperature lapse rate is -6 K/km. Precipitation from CAM is repartitioned into rain and snow as a function of near-surface temperatures (CESM, 2020; Muntjewerf, Sellevold, et al., 2020).

2.1.1.1. The snowpack

Snow/firn cover is discretized into up to 5 vertical layers (depending on the total snow thickness). New snow density is calculated based on wind and temperature. As the snow ages, parameterisations are applied for snow compaction by melt, drifting because of wind, overburden, and crystal breakdown (see section 8.6, CESM, 2020).

When melt occurs, snow is removed and converted into liquid water, which is free to percolate. If refreezing occurs, liquid water is changed into ice (section 6.2, CESM, 2020).

Water percolation though the layers is calculated explicitly using an effective porosity. Layers can become impermeable if the effective porosity becomes low enough. Temperatures are calculated in the layer first without taking phase change into account, and then adjusted when phase change is taken into account.

Finally, runoff is parameterised for lateral subsurface flow. Runoff is also forced if water on the surface exceeds a the ponding depth of 10 kg/m² (section 7.5 CESM, 2020). Melt of bare ice is not allowed to refreeze and is automatically fully taken as runoff. Finally, if the bottom snow layer transfers mass to the ice sheet whilst it contains liquid pore water, this pore water is assumed to run off (section 7 CESM, 2020).

2.1.2. CISM2

The second model component is the Community Ice Sheet Model, CISM2. Currently, only the GrIS can be modelled interactively, as CESM does not yet support all the marine interactions of a floating ice shelf, which are an important part of the Antarctic Ice Sheet and some former ice sheets.

The CISM component has a 4 km spatial resolution. On the GrIS, the snowpack is modelled by CLM. This snowpack is limited to 10m water equivalent. Any value over this limit is passed over to CISM and considered fully formed ice. CLM also calculates surface melt, which is transferred as ice ablation (negative SMB) to CISM for bare ice melt. Snow and firn mass variations between 0 and 10 m water equivalent are therefore not communicated to the ice sheet model.

To downscale inputs of net ice accumulation or net ice ablation from the 1° grid in CLM to the 4km grid in the CISM, trilinear interpolation is performed (linear between elevation classes and bilinear in the horizontal). A mass conservation correction is applied within the downscaling procedure to avoid artificial mass leaks or gains in the transfer (Muntjewerf et al., 2021).

2.1.3. CAM6

The final model component to be discussed is the Community Atmosphere Model, CAM6. CAM operates on a 6-hourly basis. It calculates simulates dynamical and thermodynamical processes in the atmosphere as well as the concentrations of various gases (water vapour, H_2O_2 and SO_2) and aerosols (such as soot and dust) through the atmosphere. It also simulates atmospheric chemistry and aerosol depositions. It also calculates cloud cover its effect on radiative fluxes (primarily the downward shortwave and upward longwave). Within the boundary layer, CAM calculates turbulent exchanges of temperature, momentum, chemicals and aerosols between the atmosphere and the land and ocean surfaces.

As default and in the simulations analyzed in this thesis, CAM operates with a 1° horizontal spatial resolution, and has 32 vertical sigma levels, with the lower boundary being determined by underlying surface topography. For the GrIS, CAM receives elevation information about the changing ice sheet topography every five years from CLM, and adjusts the elevation levels accordingly. Furthermore, CLM and CAM calculate coupled temperature and humidity fields, that are affected by the presence of a glacier surface (Craig et al., 2011).

2.2. Simulation design

Simulations	Length (time period)
3xCO_2	825
4xCO_2	1750
Hist	1950-2014

Table 2.1: Length and time period (for historical) in years for each simulation.

Among other forcings, the model needs greenhouse gas emisssions or concentrations for future climate simulations. For this thesis, two different simulations corresponding to two scenarios of greenhouse gas concen-

trations will be used.

The first scenario is denoted as $3xCO_2$. It starts off at a pre-industrial CO_2 concentration (285 ppmv - parts per million volume), that increases at a rate of 1% per year until reaching 3 times pre-industrial level (855 ppmv), after which it is kept constant (see figure 2.2). This increasing from pre-industrial to constant plateau takes 111 years and we will refer to it as the transitive phase.

The second simulation $4xCO_2$. It also starts off at a pre-industrial concentration, that increases by 1% per year until it reaches four times pre-industrial (1140 ppmv). Its transitive phase lasts 140 years. It should be noted that the first 111 years of the $3xCO_2$ and $4xCO_2$ scenarios are identical (Dickinson et al., 2000, and see figure 2.2). Both the $3xCO_2$ and $4xCO_2$ will be analysed until year 825 (when the $3xCO_2$ ends). After year 500, the output timestep changes from 1 year to 5 years.

Finally, we use one historical run, that is forced with anthropogenic GHG emissions as they occurred in the recent past. This run is used only for validation purposes. (van Kampenhout et al., 2017)

The three runs are plotted against time in (figure 2.2).

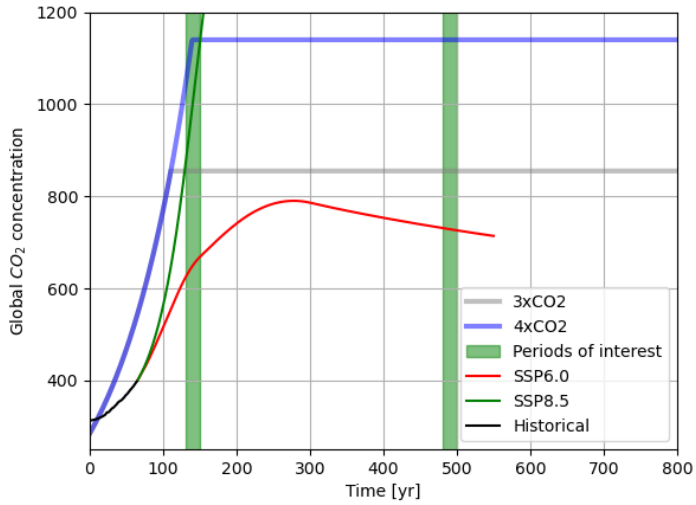

Figure 2.2: CO_2 concentration timeseries of the $3xCO_2$ and $4xCO_2$ scenarios in ppm (on the left) and as a multiple of the initial concentration of 285 ppm. Historical, SSP6.0 and SSP8.5 simulation forcing from Meinshausen et al., 2020 are plotted, with 1950 CE set as year 0.

The two scenarios share the same output for the first 110 years. The $4xCO_2$ simulation was run first, the $3xCO_2$ simulation was started with a so-called "warm restart". This means the simulation was started directly from output of a previous run. So the $3xCO_2$ simulation starts directly after year 110 of the $4xCO_2$ simulation.

In terms of model physics, the two are both two-way coupled between the GrIS and the atmosphere and land components, and one-way coupled to the ocean. The latter means that the ocean component does receive GrIS runoff from CLM and ice discharge from CISM but melting or retreat is not applied at the marine-terminating outlet glacier fronts (Muntjewerf, Sellevold, et al., 2020; Muntjewerf et al., 2021). The latter forcing explains a large part of the contemporary mass loss for the GrIS, and is considered in a parameterized way in ISMIP6 simulations for AR6 (Goelzer et al., 2020).

2.3. Transects and the K-transect

2.3.1. Transects

In order to analyse the results with respect to elevation and latitude, two transects were considered (figure 2.3).

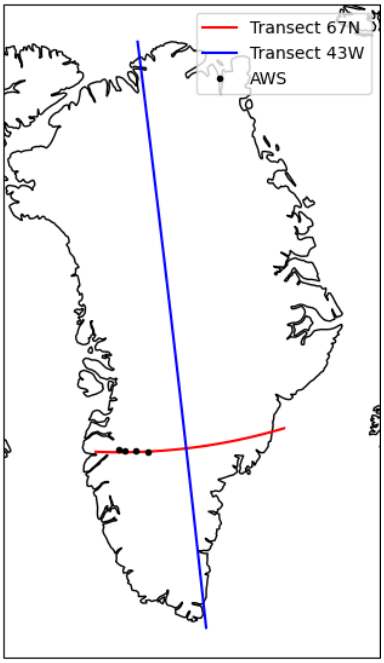

Figure 2.3: GrIS transects used for analysis in this thesis. The east-west transect is denoted as "Transect 67 N". Black dots represent the weather stations along the K-transect (section 2.3.2, Smeets et al., 2022).

The location of the transect was chosen as 67°N. 67°N was chosen as it is at the same latitude as the K-transect (Smeets et al., 2022), Atmospheric observations from four weather stations and SMB measurements from stakes along this transect are used in this thesis to evaluate the CESM-CISM model (section 3.1).

2.3.2. K-transect

Named after the nearest settlement, the Kangerlussuaq transect (k-transect) is a transect covering the western ice sheet margin at a constant latitude of about 67°N. Four automatic weather stations (AWS) are situated along the transect, as well as four additional SMB measurement locations. The SMB is measured with stakes recording surface elevation variations (Smeets et al., 2022). The AWS monitor and send the data continuously, at one-hour intervals. That data was published by van de Wal et al., 2012.

2.4. Calculation of GrIS-average Equilibrium Line Altitude

The equilibrium line is a virtual line where time-averaged (usually annual) SMB is equal to zero, meaning that there is no mass gained or lost at the surface along that line over the averaged time period. By definition, this line also separates the ablation area (where SMB is negative) from the accumulation area (where SMB is positive). In practice, whether a location gains or losses surface mass is a function of elevation. Hence an interesting variable to analyse in the context of glacier sensitivity to climate change is the evolution of the equilibrium line altitude (ELA).

Calculating a single value of the ELA is more difficult on such a large area as the GrIS, as other influences such as local climate and latitude can cause the ELA to be different locally. To calculate a GrIS-averaged ELA, we first observe the fraction of the GrIS that is ablation area (e.g. 60%). Second, we construct a hypsometric curve (a curve that shows the cumulative area distribution as a function of elevation). Thirdly, we find the elevation which has that fraction of the GrIS below it, and call that the GrIS-averaged ELA. So in our example, let's assume that 60% of the GrIS area is below 2500 m. Hence we will use this 2500m as the GrIS-averaged ELA.

3

Results

In this chapter we will evaluate the modelled elevation gradients of temperature, radiative fluxes and SMB in section 3.1, as gradients of these variables will be relevant for analysis in sections 3.4 and 3.7. We will then discuss compare the simulated global and regional climate change for the 3xCO2 and 4xCO2 simulations for 2m temperature in section 3.2. The MB, SMB and SEB will be analysed using time series, tables and maps in section 3.3 and transects in sections 3.4 respectively. Next, we will focus on refreezing on the GrIS over elevation and time (section 3.5).

Then, analysis will be performed area distribution over elevation in section 3.6. We will then research local SMB-elevation distribution in section 3.7. Finally, we will use results from sections 3.6 and 3.7 to find a theoretical framework to explain future spatial distribution of surface mass loss over the GrIS.

3.1. Model evaluation

To evaluate the model, we used freely available historical CESM2 simulation with variable ice sheet (Danabasoglu, 2019). This data was compared with mass balance observations from automatic weather stations (AWS) along the K-transect (Smeets et al., 2022).

3.1.1. Temperature variation along the K-transect

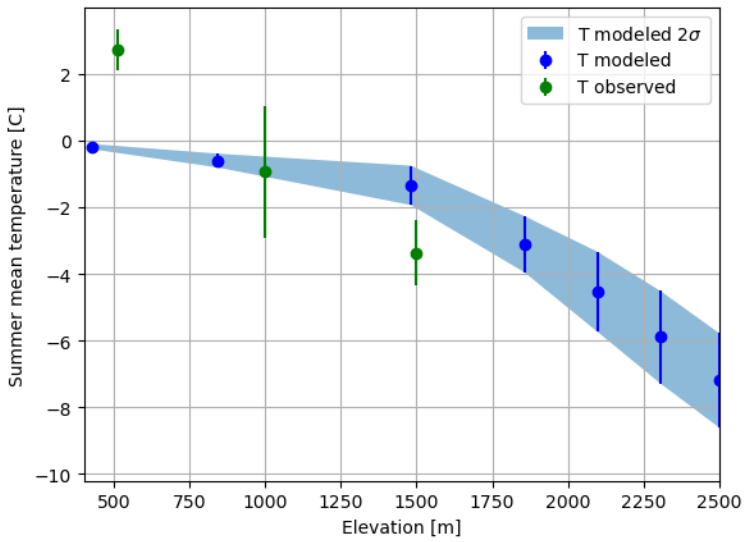

Figure 3.1: Modelled 2003-2012 mean summer 2m temperature against elevation along the K-transect from CLM. The vertical bars span 2σ of inter-annual variability.

Modelled observations in figure 3.1 have a change in temperature lapse rate around 1500 m. This coincides with the ELA, which is also situated at about 1500 m (see figure 3.15).

The observed lapse rate under the ELA is about -7 K/km, which is similar to the modelled gradient above the ELA. The modelled temperature lapse rate below the ELA is much lower, at about -2 K/km. The low lapse rate is caused by summer model surface skin temperatures being limited to 0 degrees, which in turn cools the near-surface atmosphere. However, in reality, cold surface temperature would induce a stable boundary layer (as observed by Forrer and Rotach, 1997), This means that turbulent exchanges between the surface skin and the lower atmosphere are limited. That explains why the observed temperatures deviate from the skin temperature, which is still limited to 0 °C. In short, the influence of the skin temperature on the 2m air temperature seems higher in the model than in observations.

3.1.2. Radiation at the K-transect

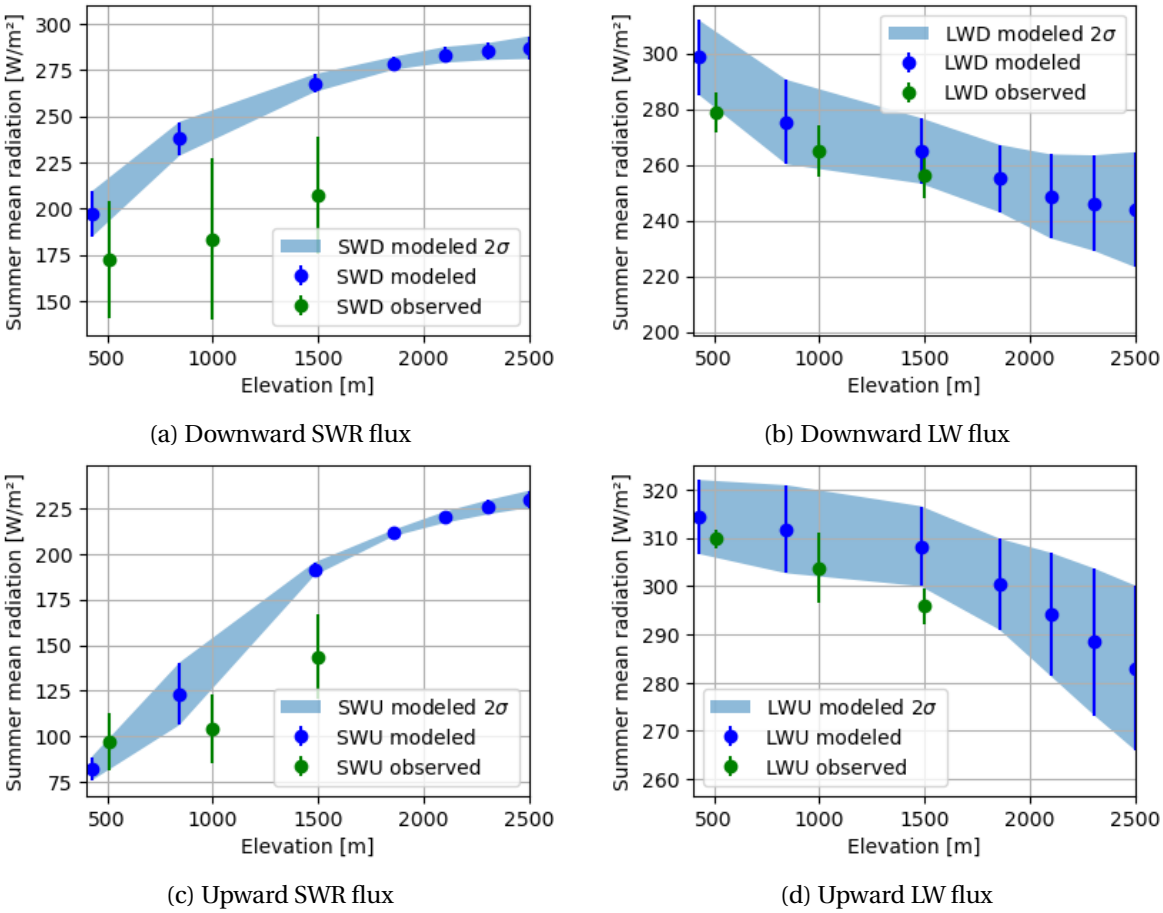

(a) Downward SWR flux

(b) Downward LW flux

(c) Upward SWR flux

(d) Upward LW flux

Figure 3.2: Summer mean radiations averaged from historical runs and k-transects observations over years 2003-2013.

Figure 3.2 shows that in both directions, the model overestimates the shortwave fluxes. This possibly indicates an underestimation of the presence of clouds. The albedo of the model and observations agree well for the 1000 and 1500 m elevations, but not at 500 m. Here, the model underestimates the albedo (see figure A.5).

den Broeke et al., 2008; Ettema et al., 2010 note that the albedo at lower point on the ice sheet is equal to that of bare ice year-round.

The longwave fluxes are also subject to the overestimation of fluxes, though the scale of the difference is slightly smaller.

The gradients in the model (exact K-transect values are in 3.5) are similar to observed gradients, with exception to the upward SWR (SWU) and albedo gradients. Furthermore, we note that observations are limited to below 1500 m, which is also where the ELA lies in model observations, therefore, we cannot compare model

behaviour above the ELA.

3.1.3. SMB at the K-transect

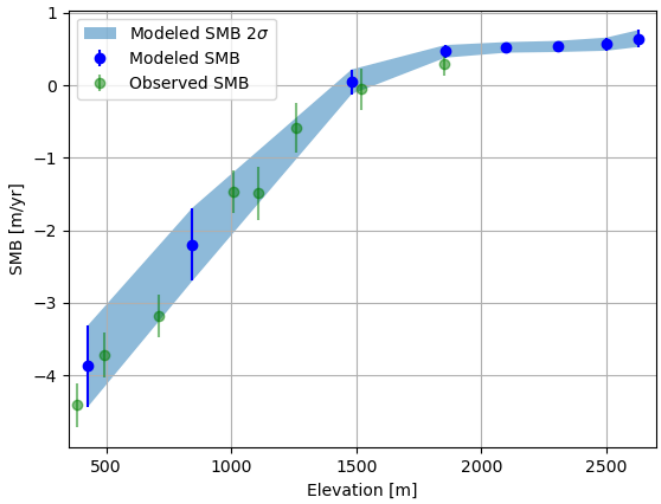

Figure 3.3: Annual SMB in m/yr from the historical run and from the K-transect, averaged over the years 2000-2010.

Figure 3.3 shows SMB modelled and observed as a function of elevation on the K-transect. SMB observations are derived from stake measurements by van de Wal et al., 2012.

Agreement between the modelled and observed SMB is good for all elevations. The same can be said for inter-annual variability (measured by the error bars), which is larger as the SMB as elevation decreases. The observed AASMB gradient is about 3.9 [m/yr/km].

3.2. Global and regional temperature anomalies

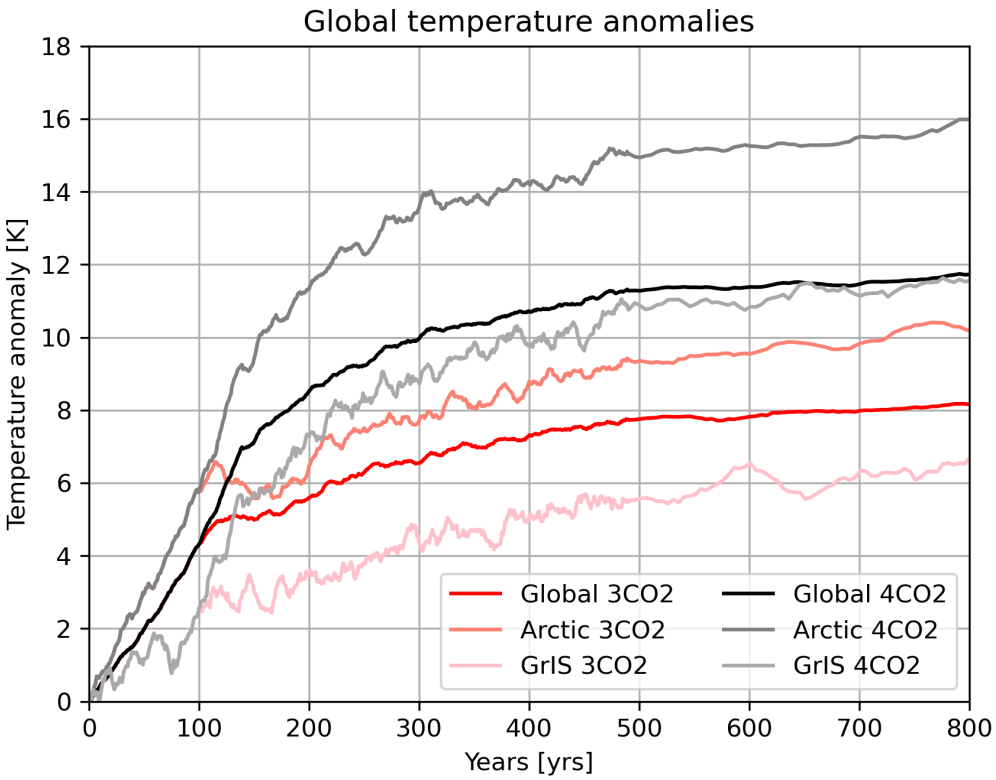

Figure 3.4: Evolution of 10-year running mean global, Arctic and Greenland ice sheet change in near-surface temperature (K) with respect to pre-industrial for 3xCO_2 (red and pink lines) and 4xCO_2 (black and grey lines). The Arctic is defined as the area north of 60 degrees N. Note that the model timestep increases from one to five years after year 500.

Figure 3.4 plots the decadal running mean temperature anomalies for the 3xCO_2 and 4xCO_2. Note that the simulation lengths differ between the 3xCO_2 (limited to 825 years) and 4xCO_2 scenarios (runs until 1800).

The simulated warming is larger in arctic than the global average for both scenarios. This can be recognised as Arctic Amplification (Rantanen et al., 2022) of global warming. The GrIS warms more slowly than the global mean. This can be explained by the fact that the GrIS acts like a thermal buffer that maintains summer 2m temperature at melt point (Muntjewerf, Sellevold, et al., 2020).

3.3. Greenland ice sheet mass and energy budgets

3.3.1. Mass Balance evolution

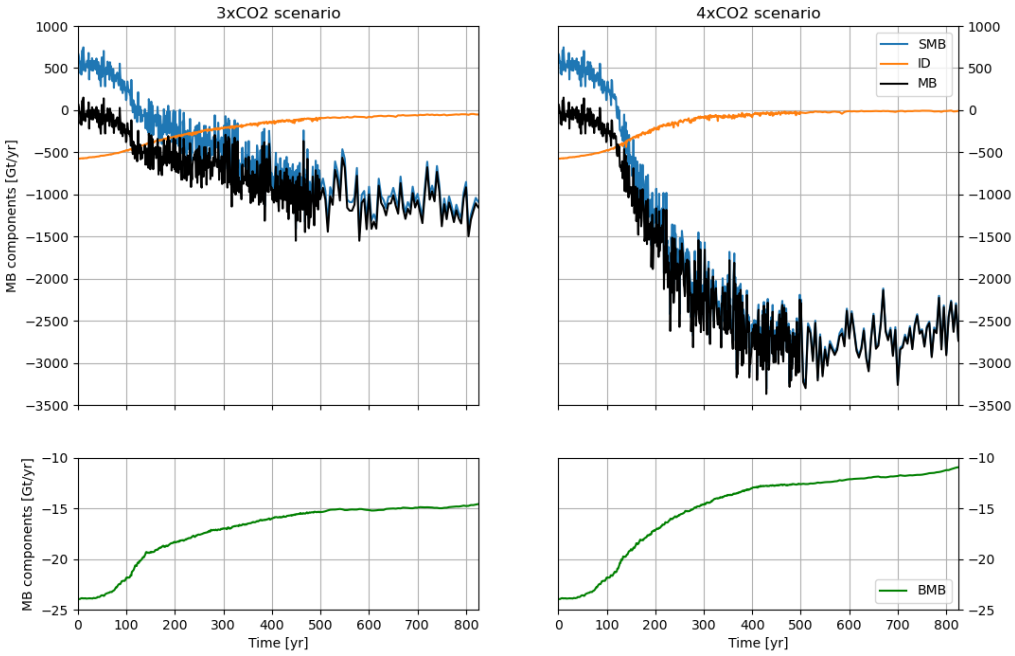

Figure 3.5: Mass balance components in the GrIS for 3xCO_2 (on the left) and 4xCO_2 scenarios (on the right) from CISM. The BMB for both scenarios is shown separately, as it is significantly smaller than the other mass fluxes.

As shown in figure 3.5, the SMB positive and is approximately equal to the mass loss caused by the ID at the beginning of the simulation. But as the CO_2 concentration increases the SMB turns negative around year 120 for both scenarios, which is accompanied with a decrease of ID. This is likely a consequence of the thinning of the ice sheet, as a thinner ice sheet discharges less towards the sea. The ice discharge continues to decrease until it effectively reaches zero. This is caused by the retreat of the ice sheet margins from the sea to further inland, where ice discharge becomes impossible. The ID is negligible for 3xCO_2 and 4xCO_2 by years 500 and 300, respectively. The BMB as modelled by CESM2.1 is relatively small and can therefore be disregarded in our analysis. Because the SMB is dominant in the mass loss of the GrIS, this research focuses on that SMB.

3.3.2. Surface Mass Balance

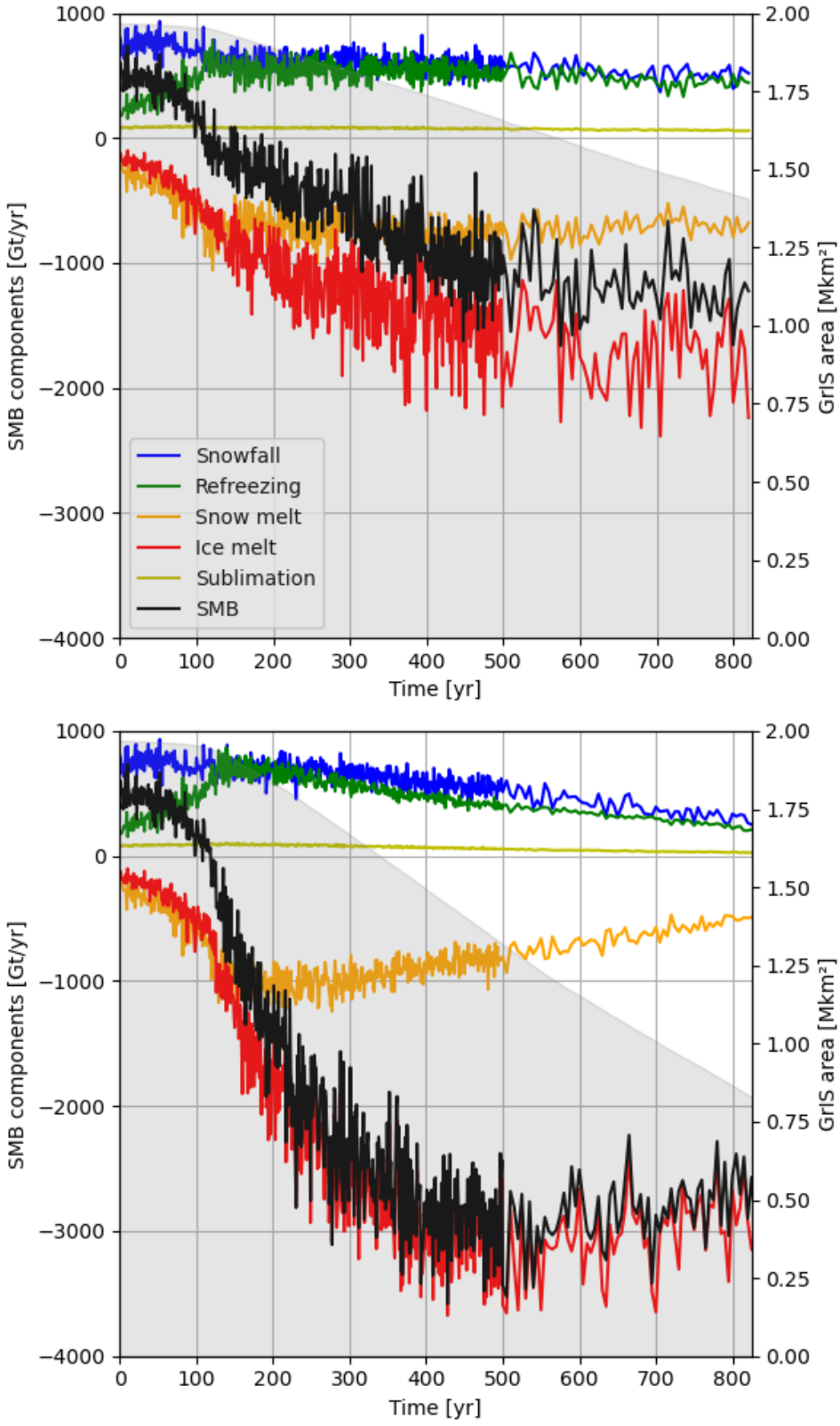

Figure 3.6: Surface Mass Balance components integrated over the GrIS for the $3xCO_2$ (top) and $4xCO_2$ (bottom) scenarios in Gt/yr (scale on the left). The timeseries of the GrIS area is represented by the gray in the background (scale on the right). Again, there are differences in timestep after year 500 that is common to all components.

Years	0-100	100-200	200-300	300-400	400-500	500-600	600-700	700-800
SMB	405	-146	-467	-732	-1020	-1101	-1222	-1184
Snowfall	748	630	618	606	581	575	520	511
Rainfall	99	143	160	184	198	210	197	204
Ice melt	299	805	1165	1337	1523	1574	1825	1644
Snow melt	405	694	721	745	760	737	724	674
Refreezing	338	550	546	543	530	501	483	436
Sublimation	88	83	81	80	75	72	66	64

Table 3.1: 100-year average SMB components in Gt/yr for the 3xCO_2 scenario. Positive SMB values add mass to the ice sheet.

Years	0-100	100-200	200-300	300-400	400-500	500-600	600-700	700-800
SMB	405	-661	-1998	-2593	-2877	-2988	-2850	-2771
Snowfall	748	708	686	626	560	488	404	334
Rainfall	99	237	375	415	435	441	390	323
Ice melt	299	1193	2271	2801	3054	3203	3055	2952
Snow melt	405	899	1021	935	837	755	660	561
Refreezing	338	652	622	515	432	377	324	268
Sublimation	88	93	86	75	62	51	42	34

Table 3.2: 100-year average SMB components for the 4xCO_2 scenario in Gt/yr. Positive SMB values add mass to the ice sheet. Note that the first column was added for completeness, it is identical to the one in 3xCO_2.

Total SMB is dependant on its components, that will each be discussed below. The areal distribtution over the GrIS is initially very similar between the 3xCO_2 and 4xCO_2 scenarios (in 130-150, figure B.2). However, this is no longer the case by the years 480-500 (figure B.2).

The snowfall decreases briefly in the first centuries of both time series (figure 3.6). For the 3xCO_2 scenario, the snowfall weakens slightly over the last 200 years of the simulation, which corresponds to the decrease in ice sheet area. Between the years 150 and 600, the snowfall remains constant despite the shrinking ice sheet area, meaning that the area-averaged snowfall increases slightly. For the 4xCO_2 scenario, the solid precipitation decreases slowly in lockstep with diminishing size of the GrIS, as it does in the 3xCO_2 scenario (see figure A.3 in the appendix).

The refreezing flux increases strongly during the period of CO_2 increase of both scenarios. This implies that the refreezing is restricted by the availability of water. After this it both areal and total refreezing stabilises to a value slightly under the snowfall, as can be seen in tables 3.1 and 3.2. The refreezing is limited to areas mostly above the ELA (figure B.3). This makes sense, as bare ice can be assumed to have no refreezing capacity.

The snow melt also increases strongly during the transitive (changing CO_2 concentration) climate phase for both scenarios. After this, area-normalised snow melt remains constant for both scenarios at about -0.35 and -0.60 m/yr for 3xCO_2 and 4xCO_2 respectively. In 3xCO_2, the snow melt this is inferior to the sum of the snowfall and refreezing flux, meaning that there is a positive snow budget that contributes to the SMB.

For the 4xCO_2 scenario, it also stabilises and by year 400 it approximately matches the magnitude of the snowfall and the refreezing together, meaning that for a large area, snow is completely melted away, exposing bare ice. This is different from the 3xCO_2 scenario where snow budget is still positive.

The ice melt increases continuously throughout the simulation for 3xCO_2. By year 400 it dominates the total SMB. There is a gap between ice melt and the total SMB caused by the positive snow budget mentioned before.

In 4xCO_2, by the year 400 as the snow melt and balances out the snow fall and refreezing, it becomes the dominant factor in the SMB. This is different than the 3xCO_2 scenario, where total SMB does not share this similitude with ice melt. This difference is a logical consequence of the snow mass budget difference noted above. By year 500 the ice melt flux decreases in 4xCO_2, as the available area to melt decreases.

Total melt is significantly lower in ablation areas (figure B.4) for both scenarios. Early in the 4xCO_2, refreezing counterbalances the melt, decreasing the size of the ablation area. However, melt at low elevations becomes very strong by the end of the 4xCO_2 scenario (figure B.4).

For both scenarios, the sublimation flux is much smaller than the other fluxes. The area-normalised sublimation is close to constant for the duration of the simulation (see figure A.3). Visually from figure 3.6, it is

does not display much inter-annual variability, both in relative and absolute terms, but it does decrease in value in tandem with the decrease of the GrIS area.

3.3.3. Surface Energy Balance

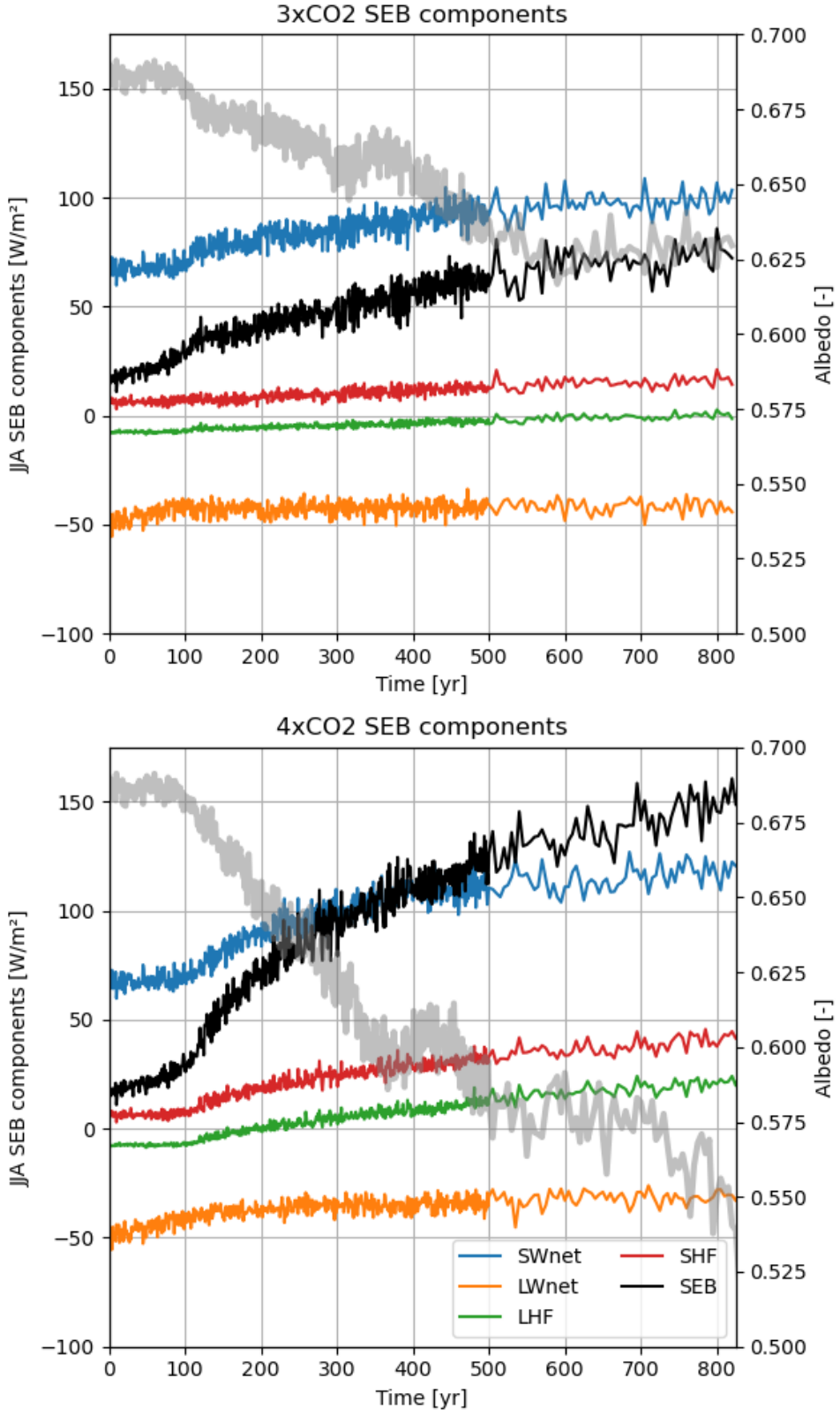

Figure 3.7: Time series of JJA energy balance in W/m² for the $3xCO_2$ scenario on the top, and for the $4xCO_2$ scenario on the bottom, averaged over the GrIS (scale on the left). On the background, the timeseries of the GrIS averaged albedo (scale on the right).

The net shortwave radiation (SWnet) initially stays constant, up to the year 100, corresponding with a constant albedo during this period. After year 100 it increases over the course of the simulation. Over the duration of the simulation, downward shortwave decreases (see figure A.4). This likely has to do with increased cloud cover, which also reflects SWR out to space. By year 500 SWnet increases more slowly in both scenarios. The de-correlation between SWnet and albedo must be because the quantity of solar radiation that reaches the ice sheet decreases due to increased cloud cover. For 3xCO_2, the albedo also stabilises at about 0.63 starting from year 500, whereas it does not in the 4xCO_2 scenario.

For both scenarios, the net longwave radiation (LWnet) increases slightly during the transitive CO_2 periods (i.e., it becomes less negative). After this, the LWnet stabilise at their new value of -40 and -30 W/m² for 3xCO_2 and 4xCO_2, respectively. The outgoing LW is a function of the temperature of the surface and its emissivity, which both increase over time (and therefore increase the outgoing longwave radiation). The only way in which the net longwave can remain stable is if the downwelling longwave radiation is increased.

The sensible heat flux (SHF) component increases because the air temperature increases whilst snow temperatures cannot exceed melt temperature. So as the air temperature above the GrIS keeps increasing (see figure 3.4), the SHF increasingly transfers heat to the GrIS. The major difference between the two scenarios is the magnitude and speed of the increase. In the 4xCO_2 scenario, a faster acceleration after year 100. By year 800, the 4xCO_2 SHF is twice as large as the 3xCO_2 SHF.

The latent heat flux (LHF) component increases and even a net energy loss to an energy gain flux in 4xCO_2. In general, the GrIS sees an increase in air temperature whilst relative humidity remains constant. This means that there is more water vapour available for deposition. And as the SHF increases, it means more mixing in the boundary layer between atmosphere and ice (visually, SHF and LHF two correlate in figure 3.7). As warm air from the atmosphere is brought into contact with the snow, it cools down, meaning that it cannot support as much water vapour. This vapour then deposes itself, releasing latent heat. This link between the SHF and LHF can be seen in the way the two correlate (which is most visible after the temporal resolution decreases, beginning in year 500). For the 4xCO_2 scenario the LHF increases even more strongly than the SHF from year 0 to 800, passing into a net positive value and then increasing until being equal to the SHF at about 30 W/m².

The total SEB represents the energy available for melt. Over time, this value increases continuously up to 75 W/m² for 3xCO_2, and up to 150 W/m² for the 4xCO_2. No single component explains this difference. All components are more positive in 4xCO_2 than in 3xCO_2. The largest relative changes were observed in the SHF and LHF, with the largest absolute change being the SWnet.

	0-100	100-200	200-300	300-400	400-500	500-600	600-700	700-800
SEB	22	36	45	52	60	66	71	71
SWnet	68	77	84	87	93	95	98	98
LWnet	-45	-42	-43	-42	-42	-41	-42	-41
SHF	6	8	9	11	12	14	15	15
LHF	-7	-6	-5	-4	-3	-2	-1	0

Table 3.3: GrIS-averaged SEB and components 3xCO_2 for each century

	0-100	100-200	200-300	300-400	400-500	500-600	600-700	700-800
SEB	22	53	84	103	116	130	137	145
SWnet	68	80	95	105	109	112	114	118
LWnet	-45	-38	-36	-35	-34	-33	-32	-32
SHF	6	14	22	27	30	35	37	40
LHF	-7	-3	3	7	10	15	18	20

Table 3.4: GrIS-averaged SEB and components 4xCO_2 for each century

3.4. Surface balance transects

3.4.1. Elevation effect on SMB

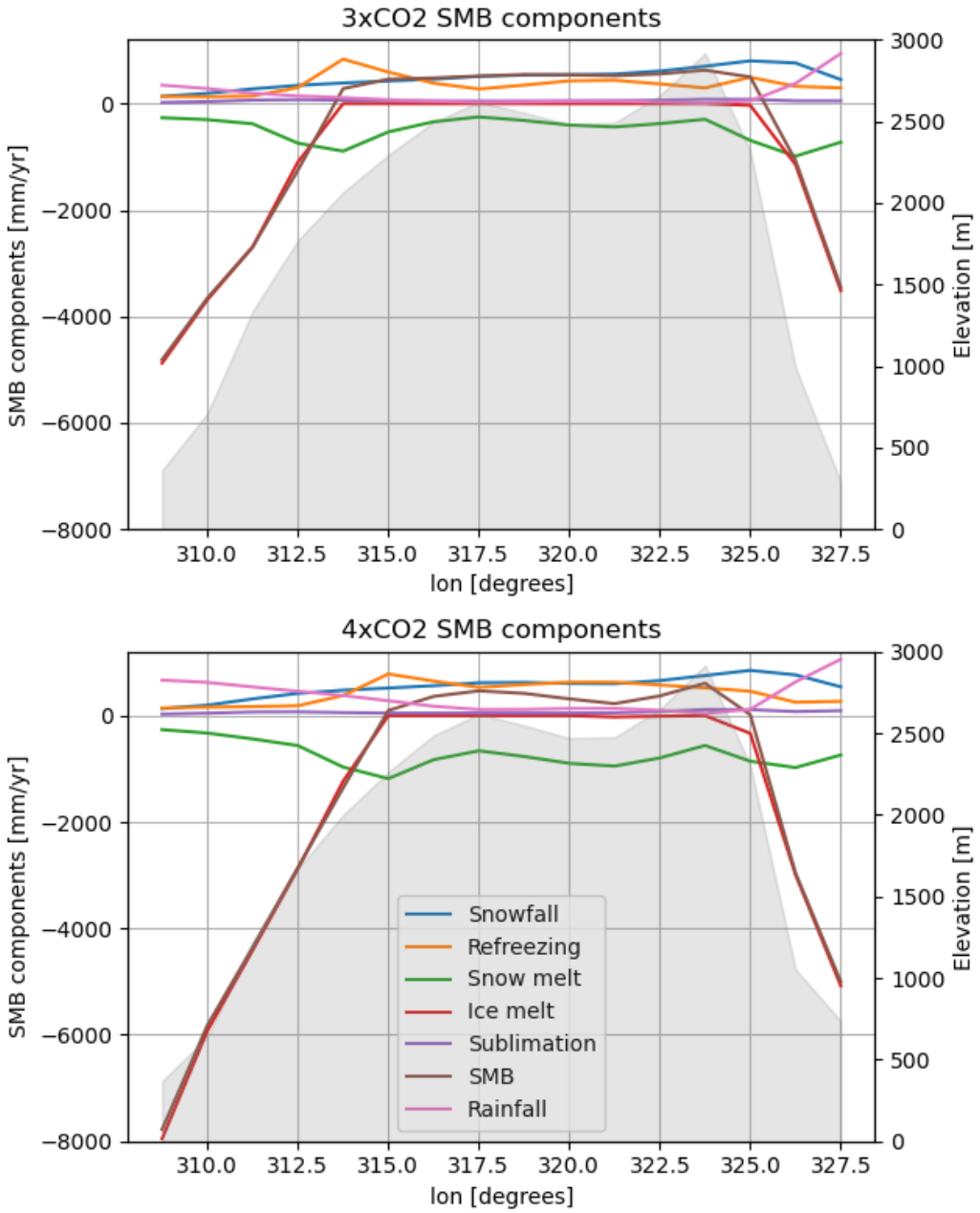

Figure 3.8: Transect of the GrIS at a latitude of 67 degrees North for $3xCO_2$ (at the top) and $4xCO_2$ (at the bottom) showing the SMB components in mm/yr averaged over years 130-150 (scale on the left). Components have positive sign if they add to the SMB and vice versa (with the addition of rainfall, which is added for indicative purposes). The gray area represents the GrIS elevation (scale on the right).

Figure 3.8 shows a transect of the GrIS at 67 degrees north for the $3xCO_2$ and $4xCO_2$ scenarios, which aligns with the K-transect. The years 130-150 were as the ice sheet morphology and ELA are still similar, but we can observe the differences in the forcing, as full $4xCO_2$ forcing has come into effect in the year 140.

Analysing the elevation of the transect, we note that the GrIS has steep edges which transition into a relatively flat plateau in the centre. The maximum elevation of this transect is approximately 3000 m. It should be noted that the edges seem cut off as the GrIS is averaged over the grid cell.

To find the equilibrium line altitude (ELA), we look for the longitude where SMB is equal to zero. In this case, this value is 312.5 degrees. This corresponds to an altitude of 1800 m. This is the ELA for 3xCO_2 in West Greenland, for the years 200 to 220. In the 4xCO_2 scenario, the ELA lies at about 2000 m.

The value for snowfall increases with elevation, and is much higher in East Greenland than in the west, owing to a difference in climate. For 3xCO_2 above the ELA, the snowfall is equal to the SMB, indicating that it is the dominant cause of mass gain on the ice sheet (as opposed to refreezing of rain). In 4xCO_2, this is no longer the case, meaning that surface melt exceeds refreezing

The refreezing flux is highest near the ELA. Above the ELA, it is equal in magnitude and opposite to the snow melt. This implies that the refreezing limited by the availability of water. Near the ELA, water is more available than above the ELA and as a consequence, refreezing spikes, before diminishing. Below the ELA in the west, the refreezing is more or less equal to snowfall, in the east, it is lower.

The snowmelt flux is also largest near the ELA. As mentioned above, at elevation superior to the ELA the snow melt balances out the refreezing. Near the ELA, the snowmelt melts the existing snowpack as well as the snowfall and refreezing. In the west, this is a significant contributor to the SMB. Below the ELA, the snowmelt is equal to the sum of the snowfall and refreezing. This implies that all available snow is melted during the melting season. In other words, this implies a seasonal snow cover.

The ice melt is zero above the ELA. Here, the snowpack still accumulates mass, meaning that any surface melt is absorbed by the snow layer. Below the ELA, the ice melt magnitude becomes very large, and dominates the surface mass balance. It accounts for a large change between the scenarios.

These very large values cause the total SMB integrated over the transect to be negative, despite the majority of area being in the accumulation zone. We note that the ice melt is larger in West Greenland than East Greenland. This is likely due to the larger snowfall and refreezing fluxes in East Greenland.

The sublimation flux is the highest near the ELA.

The transect includes the rainfall flux, as it might add mass through refreezing. We observe that it is larger at lower elevation. It is particularly high in the East. Rainfall is low above the ELA. We note that in 3xCO_2 at lon = 315 degrees, the SMB is slightly higher than the snowfall. This is likely due to a small contribution to SMB from rainfall refreezing.

3.4.2. Elevation effect on SEB

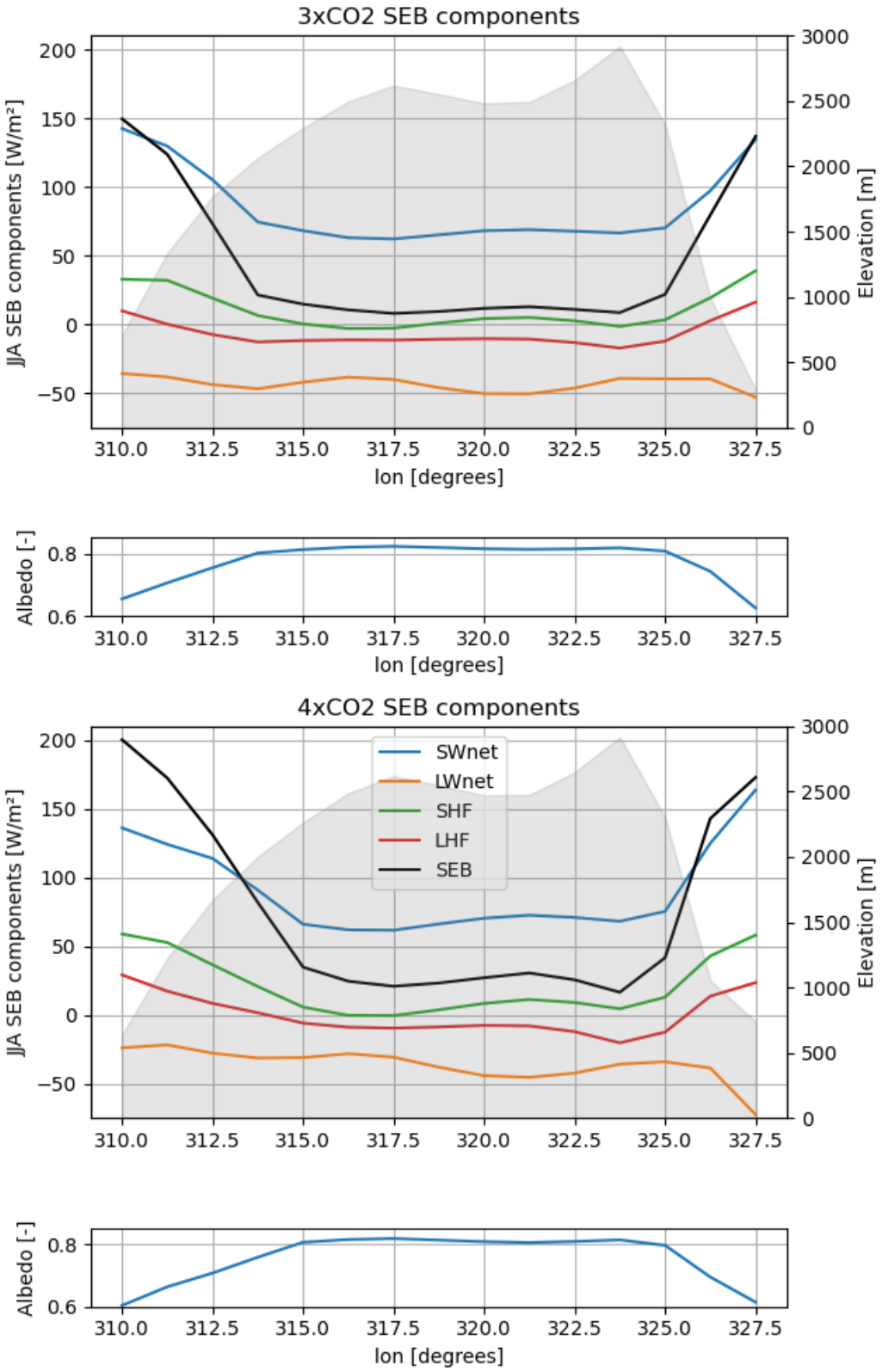

Figure 3.9: Transect of the GrIS at 67°N, showing the JJA SEB (scale on the left) and elevation (scale on the right) averaged over years 130-150 for both scenarios. Positive values add to the SEB, negative values subtract. The gray area represents the GrIS elevation. The subplots show the albedo.

As noted before, the melt is a major contributor to the SMB, which itself is a major contributor to the MB. Therefore, we will also investigate the SEB (energy available for melt) at the 67°N transect. It should be noted that the Ground Heat Flux (GHF) is small, and is therefore not taken into account.

In the figure 3.9 plots the same transect as figure 3.8, with the summer SEB components. We had concluded that the ELA lies around 1800 m for 3xCO_2 and around 2000 m for 4xCO_2.

The albedo subfigures shows that the albedo is lower below the ELA than above for both scenarios, and that the albedo is lowest in the 4xCO_2 scenario. This can clearly be seen in the effect on the SWnet, which is larger outside of the ELA than inside.

For the LWnet, we observe that centre of the transect radiates out the largest quantity of radiation. For both scenarios, the eastern edge is also a strong emitter of LW radiation, whilst the western edge is not.

These values can be explained by the two major factors in net LW: temperature and cloud cover. The high LW emissions of the eastern edge is likely due to the high temperature of the ice sheet there, and a relative lack of cloud cover. Likewise, as the highest and most continental part of the ice sheet, the cloud cover in the centre of the ice sheet is relatively thin. This allows for higher LW emissions. By contrast, the western edge is likely to have more cloud cover, which means that the outgoing LW radiation is reflected, resulting in a lower magnitude of emission.

The SHF is largest at edges of the ice sheets. This is explained by two effects. First of all, warm air must logically first cross the ice sheet edges before going inland. This means that the edges of the ice sheet come in contact with the warmest air and therefore must have larger net SHF.

Another influence of air temperature is the difference between the scenarios. The 4xCO_2 SHF is larger along the edges, likely because of larger global average temperatures (see figure 3.4). Note that this does not change the values as much at the centre of the ice sheet.

Secondly, air temperatures naturally decrease by a fixed lapse rate of about -7 K for every kilometre of elevation. Ice sheet surface temperatures are limited to melt point regardless of elevation, meaning that the temperature difference is largest at the lowest points of the glacier, the ice sheet edges.

Like for the LWnet, the effects of local climate on the SHF are visible on both edges of the GrIS. We observe that the eastern ice sheet edge has a larger SHF than the western part, and that the eastern maximum (at lon = 323.75) has a larger SHF than the western maximum (at lon = 317.5), despite having a larger elevation. We therefore conclude that eastern part of the ice sheet is warmer than the west. Finally, we will note that the elevation lapse rate explanation also helps explain the net cooling effect observed around 317.5 degrees latitude.

The LHF is most positive at low elevations, and most negative in at high elevations. This flux correlates well with elevation. Interestingly, the ELA is not the point at which the LHF changes sign. This happens below the ELA, at an elevation of about 1500 m. This elevation has no particular quality, and is likely a simple crossing point between the graphs of deposition and sublimation.

Summing up the influence of the fluxes discussed above, the SEB is relatively constant above the ELA, with some variability that can primarily be attributed to the SHF. Between the scenarios, the SHF and LHF are the main drivers of difference at this stage. Below the ELA, increases in the SHF, LHF, and especially the SWnet cause a large increase in SEB, five times the magnitude of above the ELA.

Table 1 in Sellevold et al., 2019 has values for the average downscaled gradients for the SEB for CESM1.0 and RACMO2.3. The values of found in this transect show steeper gradients than those found in Sellevold et al., 2019 (see table 3.5). For the full ice sheet, the behaviour of the gradients of both of CESM2.0's runs resemble RACMO more than CESM1.0.

Variable	Local transect		Full ice sheet	
	3xCO_2 gradient	4xCO_2 gradient	3xCO_2 gradient	4xCO_2 gradient
SWnet [W/m²/km]	-25.8	-29.6	-28.1	-29.9
LWnet [W/m²/km]	-3.48	-2.08	1.15	-2.87
SHF [W/m²/km]	-14.1	-23.4	5.84	9.25
LHF [W/m²/km]	-10.6	-15.7	-0.88	-4.33
SEB [W/m²/km]	-53.9	-70.7	-22.0	-27.8

Table 3.5: The local transect values are averaged over years 130-150, the full ice sheet covers all time steps until year 500

3.5. Refreezing

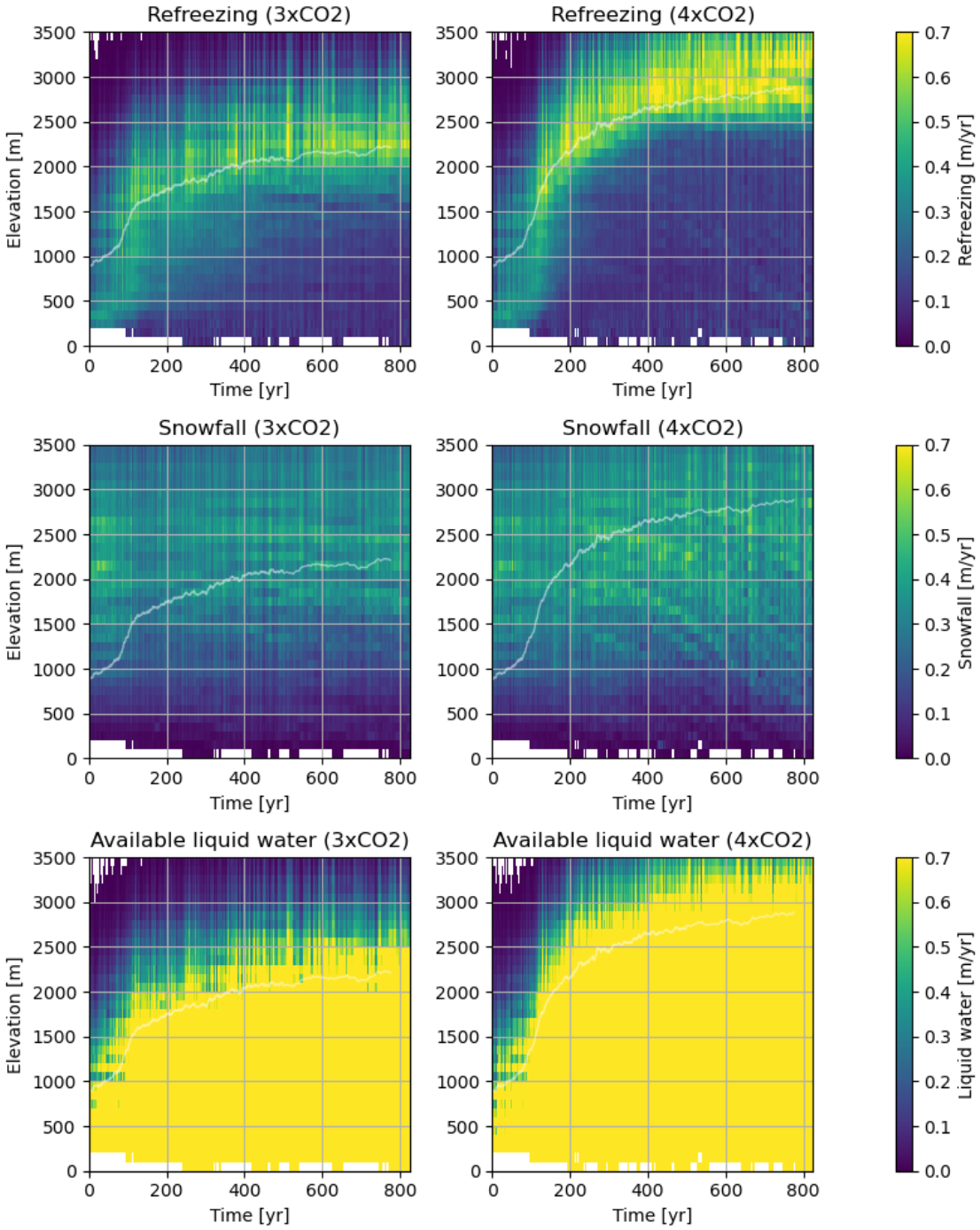

Figure 3.10: Refreezing contribution [m/yr] (top) snowfall contribution [m/yr] (middle) and available liquid water [m/yr] (bottom) separated by elevation for each year for $3xCO_2$ (left) and $4xCO_2$ (right). Note that the first 110 years are identical. The white line indicates the decadal rolling average ELA.

Figure 3.10 shows annual average (top to bottom) refreezing contribution [m/yr], snowfall [m/yr] and snow liquid water content [kg/m²] for the $3xCO_2$ (left) and $4xCO_2$ (right) over time and elevation.

After a period of initial adjustment of about 150 years, the largest refreezing rates can be found around the ELA. The upper bound of the refreezing is set by the available liquid water. For much of the ice sheet,

the available liquid water (rain + snow melt + ice melt) is not a limiting factor. Below the ELA, it is likely a combination of availability of pore space and the ability to release energy to freeze. From the middle, we can see that new snowfall alone does not generate a lower bound.

3.6. Hypsometry and orography

In this chapter we introduce the concept of ablation area expansion (section 3.6.1) and how it follows from the equilibrium line altitude (ELA) and the hypsometry of the GrIS. This approach, which is the current state of the art (e.g. Mankoff et al., 2022; Noël et al., 2019). Critiques of this model about the will be discussed in subsections 3.6.2 and 3.6.3.

3.6.1. Ablation area expansion with static hypsometry

A hypsometry is a curve representing the cumulative distribution of sub-areas within a given area over elevation. The hypsometry in figure 3.11 was calculated by sorting the ice-covered grid cell area from the CLM output by its average height, and then plotting the line created by the points $(x, y) = (\sum_{j=0}^{i} \text{area}_j, \text{elev}_i)$.

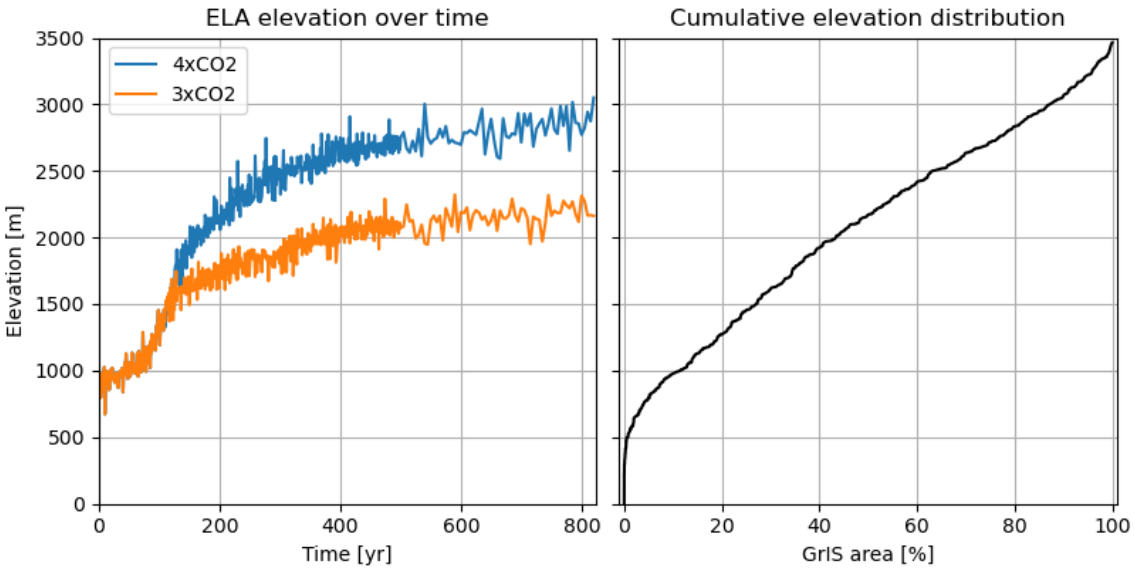

Figure 3.11: On the left: GrIS averaged equilibrium line altitude (ELA) over time. On the right: the percentage of the GrIS below a certain altitude, the hypsometric curve. The curve is made using initial elevations.

Figure 3.11 shows two interrelated effects. On the left is the altitude of the annual mean ELA as a function of time. This is obtained by taking a least squares linear regression of all grid points in the GrIS in a SMB-elevation phase space, and then selecting the value generated by SMB = 0.

On the right is a cumulative elevation distribution sorted by elevation. In other words, it shows which percentage of the GrIS is under a certain elevation.

The two graphs together can be used to approximate the fraction of the GrIS that melts for a given point in time. So for instance, in the 3xCO_2 scenario at year 400, the average annual ELA is approximately 2000 m. This corresponds to an ablation area of approximately 45% of the GrIS. If we were to take the same example for the 4xCO_2 scenario, we would see that the ELA is given as about 2650 m, and an ablation area of about 70% of the GrIS.

The leftmost figure shows that the ELA of the 4xCO_2 scenario is consistently larger than those of the 3xCO_2 scenario, starting from the year 110 when both diverge. We also see that the ELA in the 4xCO_2 scenario grows faster that its 3xCO_2 counterpart.

This means the ablation area is always larger for 4xCO_2 than for 3xCO_2. How large the difference is depends on the difference in the ELA's value as well as the cumulative distribution. If it is very steep, the area difference is relatively small. If it is shallow, it means that a change in ELA has a large impact in terms of the total ablation area.

The curve is most shallow in the range of the ELA. The curve on the right starts off very steep, implying that the GrIS has very few low-lying grid cells. Only about 10% of the GrIS lies below 1000 m. And only a further 30% lies between 1000 m and 2000 m. About half of the GrIS area lies between 2000 and 3000 m, with the remainder above 3000 m. As the ELA starts at 1600 m and climbs to 2000 m within the first 200 years for both scenarios, the shallowness of the curve 2000-3000 m range very important. Assuming that melt

increases are at least in part driven by an increase in melt area. This elevation factor is an important reason for the discrepancy observed in the mass balances of the GrIS in $3xCO_2$ and $4xCO_2$.

3.6.2. Evolving hypsometry

A criticism that can be levelled at the static hypsometry discussed in section 3.6.1 is that it only considers the initial elevation distribution. This despite that mass loss can potentially cause the distribution to change over time.

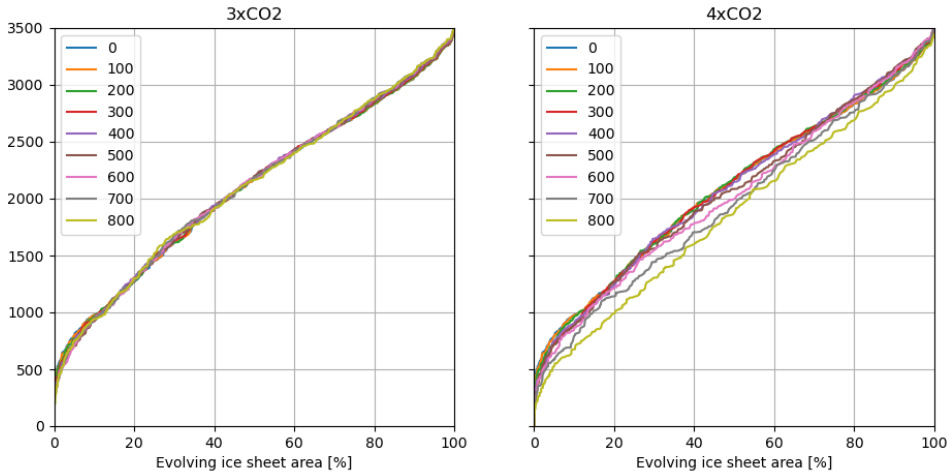

Figure 3.12: Hypsometric curves for every 100th year for the $3xCO_2$ and $4xCO_2$ scenarios. In the appendix, there is a time series of the ice sheet area A.7.

We observe that cumulative distribution of area sorted by elevation does not change substantially over time in the $3xCO_2$ simulation. It should be noted that we consider the evolving ice sheet area here.

This hypsometry does not change significantly over all time steps in the $3xCO_2$ scenario and until year 500 of the $4xCO_2$ scenario. By that year, the modelled ice sheet area is 1.65 and 1.3 Mkm² for $3xCO_2$ and $4xCO_2$ respectively, representing a 16% and 34% areal reduction relative to the initial ice sheet area (figure A.7). After that, a larger fraction of the GrIS is situated lower than in the initial situation. In other words, the GrIS becomes flatter (as can be seen when comparing maps of GrIS elevation for years 500 and 800, figure A.8). A hypsometry relative to the initial GrIS area, can be found in figure A.1.

The relatively invariant hypsometric curves imply that ice flow locally compensates the thinning at low elevations from reduced surface mass balance.

This means that evolving ice sheet hypsometry remains consistent with that plotted the figure 3.11. However, we should note that the ice sheet area changes significantly over the duration of the 825 year timespan.

3.6.3. Mass loss in elevation and in time

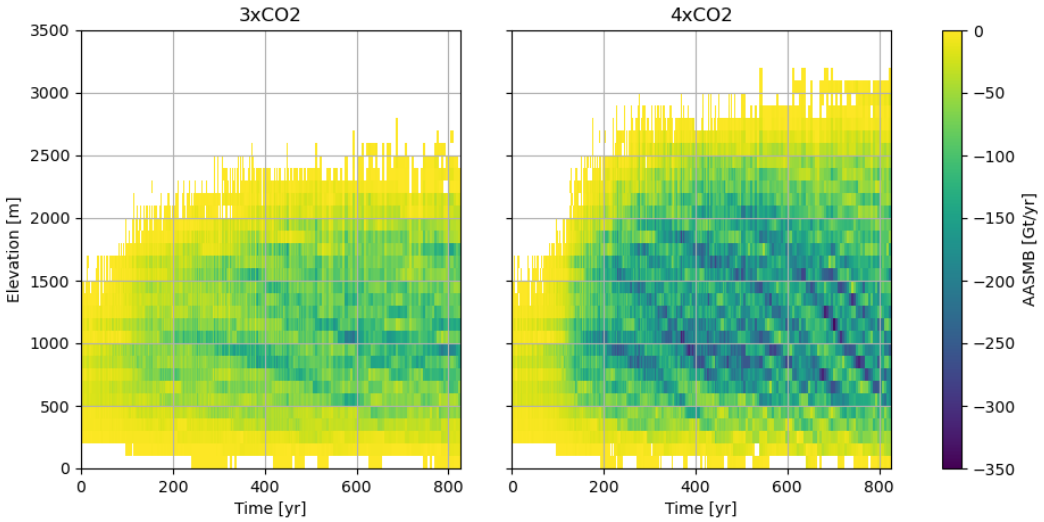

Figure 3.13: Ablation area SMB (AASMB) [Gt/yr] spilt over elevation and time for both scenarios. The accumulation area SMB is not included in this figure

Another criticism that can be levelled at the ablation area expansion model described in section ref 3.6.1 is that it does not differentiate between different parts of the ablation area. However, figure 3.13 shows that the Ablation Area SMB (AASMB) has strong variations in both elevation and time. It should be noted that only negative SMB values are plotted.

After the initial common 111 years the AASMB in the two scenarios rapidly diverge. By year 200, the ELA's upper bound for $3xCO_2$ is about 2000 m and for $4xCO_2$ it is about 2500 m. This gap of about 500 m in ELA upper bound is maintained throughout the simulation until year 825. For an area-normalised version of 3.13, see figure A.2. The area-normalised figure shows a gradient of AASMB across elevations, which we will discuss in section 3.7 (figure A.2).

3.7. AASMB-elevation distribution

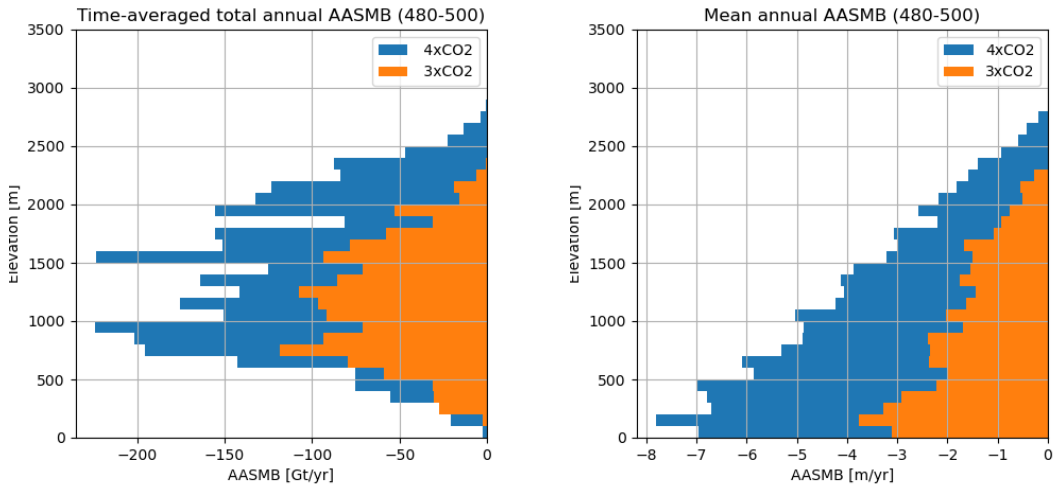

(a) Mean AASMB-elevation profile [Gt/yr]

(b) Mean AASMB-elevation profile [m/yr]

Figure 3.14: Mean ablation area SMB (AASMB) for the years 480-500 in Gt/yr, distributed over elevation. With total AASMB on the left and area-normalised AASMB on the right. An elevation-distribution graph can be found in the appendix (A.6)

Figure 3.14 shows time-averaged total AASMB split over elevations for both scenarios for the years 480-500. On the left is a version of the figure with area-normalised SMB (henceforth called "local SMB").

Above 2400 m, the SMB is above zero for all areas in $3xCO_2$ whereas it is negative for at least some areas in $4xCO_2$. However, the surface mass loss change is not concentrated above the 2400 m (or 2500 m as can be seen in tables 3.6 and 3.7. All levels see more melt from $4xCO_2$ than $3xCO_2$, which is coherent with the results from the transects discussed in section 3.4.

Below 800 m, the total melt decreases (on the left) is lower than the elevation above. This is where the ice sheet starts reaching bedrock, not due to a decrease in melt rate (as can be seen on the right). In the right-hand-side figure, local negative SMB is approximately linear with elevation. This will be discussed in 3.7.1.

Years	0-100	100-200	200-300	300-400	400-500	500-600	600-700	700-800
ELA	1030	1600	1810	1955	2071	2101	2161	2169
0-500	-14	-38	-61	-90	-98	-86	-121	-109
500-1000	-122	-258	-304	-384	-437	-436	-443	-474
1000-1500	-40	-199	-313	-330	-437	-502	-499	-470
1500-2000	-2	-55	-148	-247	-296	-315	-337	-321
2000-2500	0	-1	-4	-14	-42	-45	-54	-35
2500-3000	0	0	0	-0	-0	-0	-1	-1
3000-3500	0	0	0	0	0	0	0	0
Total	-177	-551	-830	-1064	-1310	-1383	-1455	-1411

Table 3.6: 100-year averaged AASMB in Gt/yr values by elevation in $3xCO_2$. The 100-year averaged ELA is given above for perspective.

Years	0-100	100-200	200-300	300-400	400-500	500-600	600-700	700-800
ELA	1030	1840	2339	2551	2673	2742	2779	2852
0-500	-14	-59	-147	-165	-174	-165	-196	-242
500-1000	-122	-404	-662	-706	-790	-815	-774	-781
1000-1500	-40	-383	-679	-834	-778	-820	-776	-817
1500-2000	-2	-194	-577	-704	-750	-772	-757	-573
2000-2500	0	-19	-174	-323	-472	-461	-362	-331
2500-3000	0	-0	-10	-36	-41	-52	-52	-66
3000-3500	0	0	0	0	0	-0	-1	-2
Total	-177	-1059	-2249	-2768	-3005	-3085	-2917	-2812

Table 3.7: Century averaged negative SMB in Gt/yr classed over elevation in 4xCO_2. The 100-year averaged ELA is given above for perspective. Note that due to the common forcing, the first 100 years give identical values.

Table 3.6 shows values of the AASMB in Gt/yr per elevation bin with a bin size of 500 m, starting at sea level, and averaged over the century (for the equivalent table in the accumulation area, see tables A.1 and A.2). Note that the ELA is an ice-sheet average, meaning that negative SMB values can and do occur above that elevation.

The table shows that most of the melt takes place between 500 and 1500 m of elevation for 3xCO_2 for all time steps after the year 100, also when they are far below the ELA. Mass loss is low in the lowest 500 m of the ice sheet as the ice sheet area is very small, as can be seen in figure 3.12.

It also shows that melt decreases after year 700, this is likely due to GrIS area loss (see figure 3.6).

For the 4xCO_2, seen in table 3.7, a much of the melt again takes place between 500 and 1500 m of elevation. As the ELA increases, the melt in the 1500-2000 m bin increases strongly. After the year 600, the AASMB declines significantly, likely due to the decline of the GrIS surface area that is shown in figure 3.6.

Years	0-100	100-200	200-300	300-400	400-500	500-600	600-700	700-800
3xCO_2 ELA	1030	1600	1810	1955	2071	2101	2161	2169
(a)	% of AASMB above the 3xCO_2 ELA per scenario							
3xCO_2	29	6	3	2	2	1	1	1
4xCO_2	29	12	18	18	16	14	10	11
Diff	0	17	29	31	31	26	21	23
(b)	Average ablation area [Mkm²] per scenario							
3xCO_2	0.23	0.56	0.67	0.73	0.79	0.77	0.77	0.74
4xCO_2	0.23	0.70	1.00	1.07	1.04	0.95	0.86	0.80
% diff	0	24	50	47	32	24	12	8
(c)	Average ablation area mass loss [m/yr w.e.] per scenario							
3xCO_2	-0.61	-0.92	-1.21	-1.41	-1.63	-1.76	-1.86	-1.88
4xCO_2	-0.61	-1.26	-1.90	-2.18	-2.49	-2.84	-3.08	-3.18

Table 3.8: Indicator values of melt distribution and intensity. (a) shows the percentage of AASMB above the 3xCO_2 ELA, which should be small for 3xCO_2 and larger than 4xCO_2. (b) tabulates the average ablation area size in million square km during the time period (c) shows the average local SMB in m/yr in the ablation area.

Table 3.8 shows the percentage of 3xCO_2 and 4xCO_2 AASMB that takes place above the 3xCO_2 ELA. Diff is calculated using the following equation:

$$\text{Diff} = \frac{AASMB4_{\uparrow} - AASMB3_{\uparrow}}{AASMB4_{\downarrow} - AASMB3_{\downarrow}} \cdot 100 \tag{3.1}$$

Where ↑ stands for values above the 3xCO_2 ELA and ↓ means below the 3xCO_2 ELA. This value shows that most of the change between the 3xCO_2 and 4xCO_2 scenarios takes place below the 4xCO_2 for all time steps in the table. The table also shows values for the ablation area, and values for the expansion between 3xCO_2 and 4xCO_2 (calculated as $(AA4 - AA3)/(AA3)$). Note that the AASMB increase (Diff) lags behind the ablation area expansion between 3xCO_2 and 4xCO_2.

Finally, the table shows the AASMB normalised by the ablation area, giving an average water equivalent melt rate. It is shown that negative local SMB loss is significantly higher in the ablation area in the 4xCO_2 than 3xCO_2.

The increase in local mass loss and the low increase in melt above the ELA with respect to the ablation area expansion (in the rows marked "diff") show the $3xCO_2$ ablation are the chief origin of AASMB in both scenarios.

3.7.1. Melt gradient over time

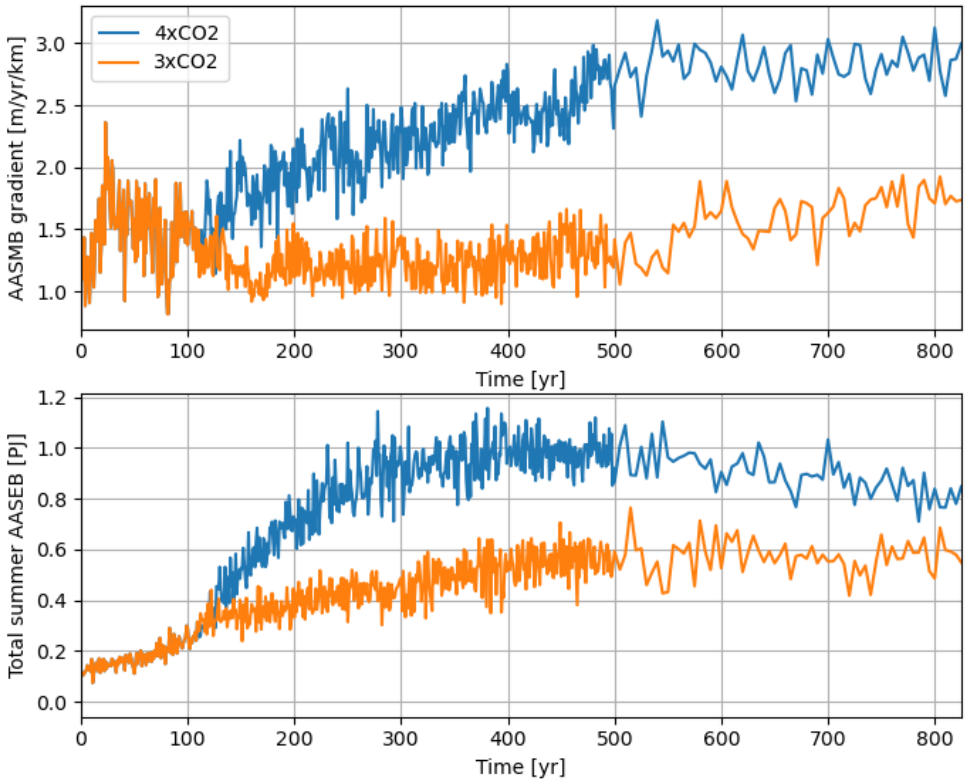

Figure 3.15: Time series of the local AASMB-elevation gradient in m/yr/km (at the top) and the integrated summer SEB in PJ (at the bottom)

As noted in the analysis of figure 3.14, the local AASMB shows a linear relationship with elevation. The top figure in 3.15 shows the time series of the local AASMB-elevation gradient in metres per year per km. The bottom figure in 3.15 is the time series of the total summer AASEB in petajoule.

The $3xCO_2$ gradient in the top subfigure is consistently less negative than the gradient for the $4xCO_2$. The $3xCO_2$ gradient also stabilises more quickly than the $4xCO_2$. This can in part be explained by the total SEB, which increases considerably over time, causing an increase in melt. This means that the SMB gradient and total SEB correlate well in $4xCO_2$ (for values after year 110, r is 0.52 and 0.73 for $3xCO_2$ and $4xCO_2$ respectively). As noted before in section 3.3.2, the snow layer on top of the ice sheet is an active contributor to the GrIS mass in $3xCO_2$. This means that more factors determine the SMB gradient than in $4xCO_2$. Therefore, the influence of the SEB magnitude is not as apparent in the local AASMB gradient.

Values of the AASMB-elevation gradient from both $3xCO_2$ and $4xCO_2$ are lower than currently observed and modelled gradients at the K-transect (which are about 3.9 m/yr/km, see figure 3.3). This is probably because of local climate.

3.8. Synthesis

This section will synthesize our findings into a final result. The first relevant conclusion so far is the linear local AASMB-gradient discussed in section 3.7.1. The second is the quasi-static evolving area hypsometry noted in section 3.6.

In order to understand the high mass loss rates that are observed as a result of high climate forcing, we look beyond the ablation area expansion. Though the ablation area increases, most of the melt increase between the two scenarios comes from points that are mass loss contributors in both scenarios, rather than in the expanded ablation area. This therefore calls for a new mental model to explain GrIS mass loss.

The new model we propose for melt is presented in equation 3.2

$$\text{AASMB(t) [Gt/yr]} = C \int_0^{\text{ELA(t)}_{\max}} \text{ELA(t)}_{\max}\text{[m/yr]} * A(t,z)dz \tag{3.2}$$

Where:

AASMB is the total mass loss over (a part of) the GrIS

C is a constant to ensure dimensional consistency with a value of 10^{-9} [Gt/m³]

AASMB(z)[m/yr] is the local AASMB as a function of elevation (like in figure 3.14b)

$A(z)$ is the area as a function of elevation, i.e., the derivative of the hypsometry.

Our analysis shows that both terms within the integral have interesting properties.

Firstly, the local AASMB is a linear function of elevation. By definition, its value should be zero at the ELA. The value of the gradient of the linear approximation differs not only in space but also significantly in time, as was shown in 3.15. We show that the gradient was steeper in 4xCO_2, meaning that SMB decreases faster as elevation decreases from the ELA.

And secondly, the area normalised hypsometry, (and therefore its derivative $A^*(z) = A(t,z)/A_{tot}(t)$) is constant up to year 500. This means that for most of the simulation, the relative distribution of the area is constant.

These two facts mean that we can rewrite equation 3.2 as follows:

$$\text{AASMB(t) [Gt/yr]} = C * A_{tot}(t) \int_0^{\text{ELA(t)}_{\max}} a(t) * (\text{ELA(t)}_{\max} - z) * A^*(z)dz \tag{3.3}$$

Where $a(t)$ is the local AASMB gradient with elevation from 3.15. We note that the $A_{tot}(t)$, $ELA(t)_{max}$ and $a(t)$ are the only time-dependant variables in the equation, meaning that they control how GrIS mass loss responds to forcing over time. Each will be discussed below.

The total area, $A_{tot}(t)$, is the most straightforward scaling. It scales the result linearly. $A_{tot}(t)$ decreases with time, meaning that it brings a small attenuation to the melt.

Using a toy model, we have determined that the influence of $A(z)$ (calculated at t = 0) at elevations between 1000 and 3000 is small, meaning that $ELA(t)_{max}$ scales the output of equation 3.3 quasi-quadratically (see figure A.10).

Finally, $a(t)$ scales the output of the equation linearly. Unlike $A_{tot}(t)$, $a(t)$ changes very strongly in time and depending on the scenario.

4

Discussion & Conclusion

In this chapter, we first discuss the novelty of this thesis and put it in context with previous research. Then we will contextualise this result using existing research. After that, a brief word about the limitations of the modelling approach used for this research are discussed. Then, to conclude, we will answer the research questions formulated in the first chapter. In order to answer the main research question, we will consider the three sub-questions in order. Finally, we will discuss some recommendations for future research.

4.1. Discussion

The main added value of this thesis is a continuation on the work of Muntjewerf, Sellevold, et al., 2020 of research into a coupled ice sheet and climate simulations. As mentioned in section 1.3, coupled ice sheet models are still rare and under development. The coupled ice sheets form the basis of the two novel iceas outlined in this thesis.

Firstly, the idea that hypsometry of an ice sheet remains constant despite strong forcing has not been produced before. Nye, 1952 derived a theoretical parabolic hypsometric shape for a circular ice cap on a flat bedrock in equilibrium. More specifically, the elevation is a function of square root of the distance to the ice sheet margin. The relationship between the two is dependent on ice material properties, such as its density and viscosity.

Our analysis shows that this pseudo-parabolic relationship does not evolve in time in transient simulations of large mass and area loss. The forcing that disrupts the hypsometry (the mass loss increase, which primarily affects the lower elevations of the ice sheet) is equilibrated by an induced forcing that redresses the heterogeneous pattern of ice thickness change. My hypothesis is that this an increased ice flow caused by a steepening of elevation gradients in the transitional area between the ablation and accumulation areas (below 1000 m in figure 3.12).

However, this relatively constant hypsometry does not last forever, as in 4xCO_2 it ceases to hold by the year 500. Furthermore, this hypsometric approach does require a large area of analysis, as ice melt can locally vary strongly (Saito et al., 2023).

Secondly, the mathematical model described by equation 3.3 that we use to explain mass loss in relationship to elevation distribution is novel. The equation does take the increase of ablation area into account through the time-dependency of the ELA. But it also takes into account the size of the ice sheet, and the changes in local SMB-elevation gradient.

This model improves on the ablation area expansion model (as used in e.g. Mankoff et al., 2022; Noël et al., 2019) in one key area: attribution. The model improves on attribution in the sense that is better able to show at which elevations mass loss is occurring most, whereas the ablation area expansion model does not distinguish between areas within the ablation area, meaning it overlooks any local difference in mass loss. Furthermore, it can also attribute mass loss changes to changes in ELA and total ice sheet area. These are both trivial, but still important from to create a holistic model.

We are not the first to find a linear relationship between local SMB and elevation in the ablation area (e.g. Oerlemans, 1991). Various other papers, some of which are tabulated in table 4.1 use this fact. All values shown in the table are for historical data, and are therefore cannot serve as a direct comparison with the results we find. It should be noted that like in our findings, authors stress that there is very strong inter-

annual variability. The values of the AASMB-elevation gradient above 77° N from Edwards et al., 2014 have a minimum value of -0.21, reversing the sign of what we commonly observe.

Paper	Value	Units	Source	Notes
Edwards et al., 2014	1.91	mm/yr/m	MAR	lat < 77° N
Edwards et al., 2014	0.56	mm/yr/m	MAR	lat > 77° N
Noël et al., 2015	3.15	mm/yr/m	AWS Observations	-
Noël et al., 2015	2.73	mm/yr/m	RACMO2.1	-
Noël et al., 2015	2.91	mm/yr/m	RACMO2.3	-
van As et al., 2017	0.0574	mm/m/day	Derived in paper	Positive Degree Day scheme
This report	1.24	mm/yr/m	CESM2.1	3xCO_2 years 130-150
This report	1.73	mm/yr/m	CESM2.1	4xCO_2 years 130-150
This report	1.31	mm/yr/m	CESM2.1	3xCO_2 years 400-500
This report	2.73	mm/yr/m	CESM2.1	4xCO_2 years 400-500

Table 4.1: Values of the ablation area local SMB-elevation gradient from literature. Please note that both MAR and RACMO are regional climate models.

As discussed in section 3.8, we found that ELA_{max} is related approximately quadratically with melt rate. Quadratic melt rates between SMB and temperature were also found by Noël et al., 2022 and Hofer et al., 2020 using data from Trusel et al., 2018. If we allow that ELA_{max} is a linear function of temperature, we might use this model to explain these findings.

4.1.1. Mathematical Elevation-SMB Model limitations

The conceptual model does inherit the limitations from the constant hypsometry. This means that the mathematical model only holds up to year 500 for the 4xCO_2 scenario, and that the model is only applicable to large areas due to strong local mass loss variations (section 4.1). In addition, the fact that the linear AASMB-elevation gradient holds for annual SMB, does not mean it holds for shorter time periods. This limits its use for the analysis short-term melt episodes. Finally, the linear local AASMB-elevation gradient is not easily measured or calculated, limiting the predictive power of the model.

This means that the model is best suited as a tool for analysis of an ice sheet or sections of an ice sheet that undergo mass loss over multiple years.

4.2. Research questions

Main question: How would future GrIS mass loss rates respond to extreme and very extreme forcing?

In section 3.3 we discussed the relative importance of total GrIS mass balance components. We mentioned that the BMB was negligible, and that the ID was modelled simplistically and became less important over time. This left the influence of the SMB as the sole research object.

1. How well do the elevation profiles of GrIS SMB and SEB components match observations on the GrIS?

We examined model performance in determining elevation gradients of 2m temperature, radiative fluxes and SMB at the K-transect. This transect is situated in West Greenland (see figure 2.3), and is sensitive to global warming as can be seen in figure B.2).

Our analysis shows that though absolute values integrated over the whole GrIS are not always well matched, gradients of the analysed variables (2m temperature, SWR and LWR fluxes) correspond reasonably well with those observed locally on the GrIS. The all-important SMB gradient along the K-transect is realistically simulated by CESM (observations: -3.9, model: -4.0 mm/yr/m). The main exceptions are 2m temperature below the ELA, which in the model does not above 0 degrees C due to the influence of the ice, but which observations show can reach above melting. This means that CESM's 2m temperature is coupled too strongly in with the skin temperature of the ice sheet. Furthermore, albedo is overestimated by the model. These are likely problems with model parameterisations.

It should be noted that values from e.g. Table 1 in Sellevold et al., 2019 demonstrate that there are very strong differences between models when it comes to predicting elevation gradients of various variables on the GrIS. For instance RACMO simulates a net-solar-radiation-elevation gradient of -19.6 W/m²/km, whereas CESM1.0 finds -3.5 W/m²/km (see Table 1 in Sellevold et al., 2019).

2. Which mass-loss related variables differ strongly between a high ($3xCO_2$) and a very high ($4xCO_2$) scenario?

Analysis of the Mass Balance components showed the SMB to be the largest component of the mass balance. Analysis of the SMB components showed that the ice melt is dominant in both scenarios. It is also one of the two drivers of mass loss difference between the two scenarios. For instance, in the years 200-300, the simulated total ice melt is 1165 and 2271 Gt/yr for $3xCO_2$ and $4xCO_2$ respectively.

The other driver of mass loss difference between $3xCO_2$ and $4xCO_2$ is mass flux from the snow budget, which is positive in the $3xCO_2$ scenario. Still for the years 200-300, the annual average flux from the snowpack is 443 and 287 Gt/yr for $3xCO_2$ and $4xCO_2$ respectively.

This difference is can be explained as follows. The ELA is significantly lower in the $3xCO_2$ scenario, meaning that a larger part of the ice sheet accumulates mass, which means that a mass flux from the snow layer to the ice sheet persists. This is in contrast to the more severe $4xCO_2$ scenario, where melt occurs over the whole ice sheet, significantly reducing the flux towards the ice sheet from the snow layer.

3. How does local SMB vary with elevation and how does that influence GrIS surface mass loss?

In section 3.6 we found that evolving area hypsometry remains constant over time for all of $3xCO_2$ and up to year 500 in $4xCO_2$. This is despite large ice sheet surface area loss.

Section 3.7.1 confirmed (previously published in Noël et al., 2019; Oerlemans, 1991) that the relationship between local AASMB and elevation when the whole GrIS is considered is approximately linear. However, we also presented results on how the simulated magnitude of this gradient changes with time. We linked this change to the total available energy.

Our analysis of local AASMB gradient in section 3.7 demonstrates that ablation area expansion explains a relatively small fraction of the melt increase. For instance in the years 480-500, the difference between the two scenarios above the $3xCO_2$ ELA (where there is little negative SMB in the $3xCO_2$ scenario) is only 23% of the total difference (391 Gt/yr above the ELA and 1332 Gt/yr below). This is smaller than the ablation area increase between the two scenarios (0.78 and 1.00 Mkm² for $3xCO_2$ and $4xCO_2$ respectively, a 28% increase, see table 4.2).

Scenario	$3xCO_2$	$4xCO_2$	$4xCO_2$-$3xCO_2$
Year	480-500	480-500	480-500
ELA [m]	1955	2551	596
GrIS area [Mkm²]	1.69	1.37	-0.32
Ablation area [Mkm²]	0.78	1.00	0.22
Ablation area [%]	43	77	-
AASMB above $3xCO_2$ avg ELA [Gt/yr]	-23	-414	-391
AASMB below $3xCO_2$ avg ELA [Gt/yr]	-1298	-2630	-1332

Table 4.2: Values of the ELA, ablation area and AASMB. Note that the AASMB above the ELA is not exactly zero as the ELA is averaged over the GrIS.

This difference is achieved by changes in melt rate in ablation area as found in section 3.7.1.

Finally in section 3.8 we link the main model results mentioned above into a novel formula (equation 4.1)

$$\text{AASMB(t) [Gt/yr]} = C * A_{tot}(t) \int_0^{\text{ELA(t)}_{\max}} a(t) * (\text{ELA(t)}_{\max} - z) * A^*(z) dz \tag{4.1}$$

Main question: How would future GrIS mass loss rates respond to extreme and very extreme forcing?

The formula in equation 4.1 gives a new perspective in the surface mass loss for a relatively constant hypsometric profile until the year 500 in $4xCO_2$, and for all time steps in $3xCO_2$. Using the formula, we will be discussing our periods of interest: 130-150, 480-500 and after year 500. We remind the reader that before the year 110, both scenarios have a common start.

In the years 130-150, the difference between the $3xCO_2$ and $4xCO_2$ is mainly caused by $a(t)$. At this point both the ice sheet area (figure A.7) and the values for ELA_{max} (figure A.9) are very similar between the two scenarios. In contrast, $a(t)$ has already diverged between the two scenarios (figure 3.15).

In the years 480-500, the difference between $3xCO_2$ and $4xCO_2$ SMB is at its largest (figure 3.6). At this point, the difference in ice sheet area is large (figure A.7), but does not dominate the two other factors, as that would have led to a smaller difference total SMB. The difference in ice sheet area contributes a decrease of

about 27% of 4xCO_2 with respect to 3xCO_2. In years 480-500, $a(t)$ causes a large difference, as the difference in gradient is about 1.5 m/yr/km in favour of 4xCO_2. This difference causes a doubling of the SMB mass loss in 4xCO_2 with respect to 3xCO_2. Finally, the average values for ELA_{max} are 2500 and 2800 m (figure A.9). Using our toy model, we find that all else being equal, the ELA's influence adds 38% to the 4xCO_2 total SMB with respect to the 3xCO_2 SMB.

After year 500, the 4xCO_2 scenario is no longer well represented by the model, as the hypsometry becomes very different from the initial hypsometry. However, from the increase of the SMB we can conclude that the attenuating effect of the ice sheet area becomes a dominant factor (figure 3.6). The local SMB keeps increasing (figure A.3). This makes sense, as we had observed that the SMB "flattens", meaning that the elevation of the ice sheet decreases (section 3.6.2), causing higher surface melt (section 3.7). These trends continue until the year 825.

As for the 3xCO_2 scenario, $a(t)$ increases a bit, and so does the ELA, meaning that there is a further decrease in both local and global SMB, until the end of its simulation, in year 825.

4.3. Recommendations

For further research, we would recommend the following topics

Application of the equation

Firstly, we would be interested in applications of the model described by equation 3.3. As was discussed in section 4.1.1, there seems to be an interesting application would be an explanation of why SMB relates quadratically with temperature (e.g. Hofer et al., 2020).

Another interesting application would be looking into the sub-regions present on the GrIS, and to examine whether regional climate (e.g. in basins from Rignot & Mouginot, 2012) can be properly captured by the model.

Hypsometric collapse

Next, we would be interested in further research into the transition of the GrIS away from the pseudo-parabolic hypsometry predicted by Glen's law that was observed from year 500 onward in the 4xCO_2 scenario in figure 3.12. What are the causes of this change in hypsometry? What are its effects on the GrIS mass loss? Does it also occur 3xCO_2?

Refreezing

In this thesis, refreezing evolution is compared for the 3xCO2 and 4xCO2 scenarios. Though we have clearly shown a link between available meltwater and refreezing, I would still be interested in the primary limitation for refreezing at low elevations. Is this temperature or pore space?

Bibliography

Alley, R. B., Andrews, J., Brigham-Grette, J., Clarke, G., Cuffey, K., Fitzpatrick, J., Funder, S., Marshall, S., Miller, G., Mitrovica, J., Muhs, D., Otto-Bliesner, B., Polyak, L., & White, J. (2010). History of the greenland ice sheet: Paleoclimatic insights [Special Theme: Arctic Palaeoclimate Synthesis (PP. 1674-1790)]. *Quaternary Science Reviews*, *29*(15), 1728–1756. https://doi.org/https://doi.org/10.1016/j.quascirev.2010.02.007

Aschwanden, A., Fahnestock, M., Truffer, M., Brinkerhoff, D., Hock, R., Khroulev, C., Mottram, R., & Khan, S. (2019). Contribution of the greenland ice sheet to sea level over the next millennium. *Science Advances*, *5*, eaav9396. https://doi.org/10.1126/sciadv.aav9396

Bamber, J. L., Griggs, J. A., Hurkmans, R. T. W. L., Dowdeswell, J. A., Gogineni, S. P., Howat, I., Mouginot, J., Paden, J., Palmer, S., Rignot, E., & Steinhage, D. (2013). A new bed elevation dataset for greenland. *The Cryosphere*, *7*(2), 499–510. https://doi.org/10.5194/tc-7-499-2013

Box, J. E., Fettweis, X., Stroeve, J. C., Tedesco, M., Hall, D. K., & Steffen, K. (2012). Greenland ice sheet albedo feedback: Thermodynamics and atmospheric drivers. *The Cryosphere*, *6*(4), 821–839. https://doi.org/10.5194/tc-6-821-2012

CESM. (2020). *Clm5 documentation* (tech. rep.). NCAR. https://web.archive.org/web/20230505095115/https://www2.cesm.ucar.edu/models/cesm2/land/CLM50_Tech_Note.pdf

Chen, X., Zhang, X., Church, J. A., Watson, C. S., King, M. A., Monselesan, D., Legresy, B., & Harig, C. (2017). The increasing rate of global mean sea-level rise during 1993–2014. *Nature Climate Change*, *7*, 492–495. https://doi.org/10.1038/nclimate3325

Craig, C., Bacmeister, J., Callaghan, P., Eaton, B., Gettelman, A., Goldhaber, S., Hannay, C., Herrington, A., Lauritzen, P., McInerney, J., Medeiros, B., Mills, M., Neale, R., Tilmes, S., Truesdale, J., Vertenstein, M., & Vitt, F. (2011). *Cam6.3 user's guide*. https://ncar.github.io/CAM/doc/build/html/users_guide/

Danabasoglu, G., Lamarque, J.-F., Bacmeister, J., Bailey, D. A., DuVivier, A. K., Edwards, J., Emmons, L. K., Fasullo, J., Garcia, R., Gettelman, A., Hannay, C., Holland, M. M., Large, W. G., Lauritzen, P. H., Lawrence, D. M., Lenaerts, J. T. M., Lindsay, K., Lipscomb, W. H., Mills, M. J., ... Strand, W. G. (2020). The community earth system model version 2 (cesm2) [e2019MS001916 2019MS001916]. *Journal of Advances in Modeling Earth Systems*, *12*(2), e2019MS001916. https://doi.org/https://doi.org/10.1029/2019MS001916

Danabasoglu, G. (2019). *Ncar cesm2 model output prepared for cmip6 ismip6 historical-withism*. https://esgf-node.llnl.gov/search/cmip6/

de Boer, B., Stocchi, P., Whitehouse, P. L., & van de Wal, R. S. (2017). Current state and future perspectives on coupled ice-sheet – sea-level modelling. *Quaternary Science Reviews*, *169*, 13–28. https://doi.org/https://doi.org/10.1016/j.quascirev.2017.05.013

den Broeke, M. R., Smeets, P., Ettema, J., & Munneke, P. K. (2008). Surface radiation balance in the ablation zone of the west greenland ice sheet. *Journal of Geophysical Research*, *113*. https://webspace.science.uu.nl/~kuipe117/docs/Broeke2008a.pdf

Dickinson, R., Gent, P., Kiehl, N. J., Moritz, N. R., & Randall, D. (2000). Community climate system model plan (2000-2005).

Edwards, T. L., Fettweis, X., Gagliardini, O., Gillet-Chaulet, F., Goelzer, H., Gregory, J. M., Hoffman, M., Huybrechts, P., Payne, A. J., Perego, M., Price, S., Quiquet, A., & Ritz, C. (2014). Probabilistic parameterisation of the surface mass balance–elevation feedback in regional climate model simulations of the greenland ice sheet. *The Cryosphere*, *8*(1), 181–194. https://doi.org/10.5194/tc-8-181-2014

Ettema, J., van den Broeke, M. R., van Meijgaard, E., van de Berg, W. J., Box, J. E., & Steffen, K. (2010). Climate of the greenland ice sheet using a high-resolution climate model. *The Cryosphere*, *4*, 511–527. https://tc.copernicus.org/articles/4/511/2010/tc-4-511-2010.pdf

Flato, G. M. (2011). Earth system models: An overview. *WIREs Climate Change*, *2*. https://wires.onlinelibrary.wiley.com/doi/pdf/10.1002/wcc.148

Forrer, J., & Rotach, M. (1997). On the turbulence structure in the stable boundary layer over the greenland ice sheet. *Boundary-Layer Meteorology*, *85*, 111–136. https://doi.org/10.1023/A:1000466827210

Fox-Kemper, B., Hewitt, H. T., Xiao, C., Aðalgeirsdóttir, G., Drijfhout, S. S., Edwards, T. L., Golledge, N. R., Hemer, M., Kopp, R. E., Krinner, G., Mix, A., Notz, D., Nowicki, S., Nurhati, I. S., Ruiz, L., Sallée, J.-B., Slangen, A. B. A., & Yu, Y. (2021). *Ocean, cryosphere and sea level change. in: Climate change 2021: The physical 12 science basisocean, cryosphere and sea level change.* (tech. rep.) [Contribution of Working Group I to the Sixth Assessment Report of the Intergovernmental Panel on Climate Change [V. Masson-Delmotte, P. Zhai, A. Pirani, S. L. Connors, C. Péan, S. Berger, N. Caud, Y. Chen, L. Goldfarb, M. I. Gomis, M. Huang, K. Leitzell, E. Lonnoy, J.B.R. Matthews, T. K. Maycock, T. Waterfield, O. Yelekçi, R. Yu and B. Zhou (eds.)]]. IPCC. Cambridge University Press. https://doi.org/10.1017/9781009157896.011.

Gardner, A. S., & Sharp, M. J. (2010). *A review of snow and ice albedo and the development of a new physically based broadband albedo parameterization.* https://doi.org/10.1029/2009JF001444

Goelzer, H., Nowicki, S., Payne, A., Larour, E., Seroussi, H., Lipscomb, W. H., Gregory, J., Abe-Ouchi, A., Shepherd, A., Simon, E., Agosta, C., Alexander, P., Aschwanden, A., Barthel, A., Calov, R., Chambers, C., Choi, Y., Cuzzone, J., Dumas, C., … van den Broeke, M. (2020). The future sea-level contribution of the greenland ice sheet: A multi-model ensemble study of ismip6. *The Cryosphere*, *14*(9), 3071–3096. https://doi.org/10.5194/tc-14-3071-2020

Hanna, E., Fettweis, X., Mernild, S. H., Cappelen, J., Ribergaard, M. H., Shuman, C. A., Steffen, K., Wood, L., & Mote, T. L. (2014). Atmospheric and oceanic climate forcing of the exceptional greenland ice sheet surface melt in summer 2012. *International Journal of Climatology*, *34*(4), 1022–1037. https://doi.org/https://doi.org/10.1002/joc.3743

Hofer, S., Lang, C., Amory, C., Kittel, C., Delhasse, A., Tedstone, A., & Fettweis, X. (2020). Greater greenland ice sheet contribution to global sea level rise in cmip6. *Nature Communications*, *11*, 6289. https://doi.org/10.1038/s41467-020-20011-8

Lenton, T. M., Held, H., Kriegler, J. W., Elmar Hall, Lucht, W., Rahmstorf, S., & Schellnhuber, H. J. (2008). Tipping elements in the earth's climate system. *PNAS*, *105*, 1786–1793. https://www.pnas.org/doi/full/10.1073/pnas.0705414105

Lipscomb, W. H., Price, S. F., Hoffman, M. J., Leguy, G. R., Bennett, A. R., Bradley, S. L., Evans, K. J., Fyke, J. G., Kennedy, J. H., Perego, M., Ranken, D. M., Sacks, W. J., Salinger, A. G., Vargo, L. J., & Worley, P. H. (2019). Description and evaluation of the community ice sheet model (cism) v2.1. *Geoscientific Model Development*, *12*(1), 387–424. https://doi.org/10.5194/gmd-12-387-2019

Lunt, D. J., Foster, G. L., Haywood, A. M., & Stone, E. J. (2008). Late pliocene greenland glaciation controlled by a decline in atmospheric co2 levels. *Nature*, *454*, 1102–1105. https://www.nature.com/articles/nature07223

Madsen, M. S., Yang, S., Aðalgeirsdóttir, G., Svendsen, S. H., Rodehacke, C. B., & Ringgaard, I. M. (2022). The role of an interactive greenland ice sheet in the coupled climate-ice sheet model ec-earth-pism. *Climate Dynamics*, *59*, 1189–1211. https://doi.org/10.1007/s00382-022-06184-6

Mankoff, K. D., Wehrlé, A., Noël, B., van den Broeke, M. R., Wouters, B., Bjørk, A. A., & Fausto, R. S. (2022). Greenland ice sheet climate disequilibrium and committed sea-level rise. *Nature Climate Change*, *12*, 808–813. https://doi.org/10.1038/s41558-022-01441-2

Maslin, M., Li, X., Loutre, M.-F., & Berger, A. (1998). The contribution of orbit forcing to the progressive intensification of northern hemisphere glaciation. *Quaternary Science Reviews*, *17*(4), 411–426. https://doi.org/https://doi.org/10.1016/S0277-3791(97)00047-4

Meinshausen, M., Nicholls, Z. R. J., Lewis, J., Gidden, M. J., Vogel, E., Freund, M., Beyerle, U., Gessner, C., Nauels, A., Bauer, N., Canadell, J. G., Daniel, J. S., John, A., Krummel, P. B., Luderer, G., Meinshausen, N., Montzka, S. A., Rayner, P. J., Reimann, S., … Wang, R. H. J. (2020). The shared socio-economic pathway (ssp) greenhouse gas concentrations and their extensions to 2500. *Geoscientific Model Development*, *13*(8), 3571–3605. https://doi.org/10.5194/gmd-13-3571-2020

Mouginot, J., Rignot, E., Bjørk, A. A., Broeke, M. v. d., Millan, R., Morlighem, M., Noël, B., Scheuchl, B., & Wood, M. (2019). Forty-six years of greenland ice sheet mass balance from 1972 to 2018. *PNAS*, *116*, 9239–9244. https://www.pnas.org/doi/10.1073/pnas.1904242116#supplementary-materials

Muntjewerf, L., Sellevold, R., Vizcaino, M., da Silva, C. E., Petrini, M., Thayer-Calder, K., Scherrenberg, M. D. W., Bradley, S. L., Katsman, C. A., Fyke, J., Lipscomb, M., W. H. andverstrom, & Sacks, W. J. (2020). Accelerated greenland ice sheet mass loss under high greenhouse gas forcing as simulated by the coupled cesm2.1-cism2.1. *Journal of Advances in Modelling Earth Systems*, *12*. https://doi.org/https://doi.org/10.1029/2019MS002031

Muntjewerf, L., Petrini, M., Vizcaino, M., Ernani da Silva, C., Sellevold, R., Scherrenberg, M. D. W., Thayer-Calder, K., Bradley, S. L., Lenaerts, J. T. M., Lipscomb, W. H., & Lofverstrom, M. (2020). Greenland ice sheet contribution to 21st century sea level rise as simulated by the coupled cesm2.1-cism2.1 [e2019GL086836 10.1029/2019GL086836]. *Geophysical Research Letters*, *47*(9), e2019GL086836. https://doi.org/https://doi.org/10.1029/2019GL086836

Muntjewerf, L., Sacks, W., Lofverstrom, M., Fyke, J., Lipscomb, W., Ernani da Silva, C., Vizcaino, M., Thayer-Calder, K., T. M. Lenaerts, J., & Sellevold, R. (2021). Description and demonstration of the coupled community earth system model v2 – community ice sheet model v2 (cesm2-cism2). *Journal of Advances in Modeling Earth Systems*, *13*(6), 1–23. https://doi.org/10.1029/2020MS002356

Nghiem, S. V., Hall, D. K., Mote, T. L., Tedesco, M., Albert, M. R., Keegan, K., Shuman, C. A., DiGirolamo, N. E., & Neumann, G. (2012). The extreme melt across the greenland ice sheet in 2012. *Geophysical Research Letters*, *39*. https://agupubs.onlinelibrary.wiley.com/doi/10.1029/2012GL053611

Nilsson, J., Vallelonga, P., Simonsen, S. B., Sørensen, L. S., Forsberg, R., Dahl-Jensen, D., Hirabayashi, M., Goto-Azuma, K., Hvidberg, C. S., Kjær, H. A., & Satow, K. (2015). Greenland 2012 melt event effects on cryosat-2 radar altimetry. *Geophysical Research Letters*, *42*(10), 3919–3926. https://doi.org/https://doi.org/10.1002/2015GL063296

Noël, B., van de Berg, W. J., van Meijgaard, E., Kuipers Munneke, P., van de Wal, R. S. W., & van den Broeke, M. R. (2015). Evaluation of the updated regional climate model racmo2.3: Summer snowfall impact on the greenland ice sheet. *The Cryosphere*, *9*(5), 1831–1844. https://doi.org/10.5194/tc-9-1831-2015

Noël, B., van Kampenhout, L., Lenaerts, J. T. M., van de Berg, W. J., & van den Broeke, M. R. (2021). A 21st century warming threshold for sustained greenland ice sheet mass loss [e2020GL090471 2020GL090471]. *Geophysical Research Letters*, *48*(5), e2020GL090471. https://doi.org/https://doi.org/10.1029/2020GL090471

Noël, B., Lenaerts, J. T. M., Lipscomb, W. H., Thayer-Calder, K., & van den Broeke, M. R. (2022). Peak refreezing in the greenland firn layer under future warming scenarios. *Nature Communications*, *13*, 6870. https://doi.org/10.1038/s41467-022-34524-x

Noël, B., van de Berg, W. J., Lhermitte, S., & van den Broeke, M. R. (2019). Rapid ablation zone expansion amplifies north greenland mass loss. *Science Advances*, *5*(9), 123. https://doi.org/10.1126/sciadv.aaw0123

Nye, J. (1952). The mechanics of glacier flow. *Journal of Glaciology*, 82–93. https://www.researchgate.net/profile/John-Nye-5/publication/224962689_Mechanics_of_glacier_flow/links/004635243f41372c4e000000/Mechanics-of-glacier-flow.pdf

Oerlemans, J. (1991). The mass balance of the greenland ice sheet:sensitivity to climate change as revealed byenergy-balance modelling. *The Holocene*, *1*, 40–49. https://dspace.library.uu.nl/bitstream/handle/1874/22284/oerlemans_91_massbalanceofthegreenlandicesheet.pdf;sequence=1

Rantanen, M., Karpechko, A. Y., Lipponen, A., Nordling, K., Hyvärinen, O., Ruosteenoja, K., Vihma, T., & Laaksonen, A. (2022). The arctic has warmed nearly four times faster than the globe since 1979. *Communications Earth & Environment*, *3*, 168. https://doi.org/10.1038/s43247-022-00498-3

Ridley, J., Gregory, J., Huybrechts, P., & Lowe, J. (2009). Thresholds for irreversible decline of the greenland ice sheet. *Climate Dynamics*, *35*, 1049–1057. https://doi.org/10.1007/s00382-009-0646-0

Rignot, E., & Mouginot, J. (2012). Ice flow in greenland for the international polar year 2008–2009. *Geophysical Research Letters*, *L11501*, 39. https://doi.org/10.1029/2012GL051634

Rutt, I. C., Hagdorn, M., Hulton, N. R. J., & Payne, A. J. (2009). The glimmer community ice sheet model. *Journal of Geophysical Research*. https://doi.org/https://doi.org/10.1029/2008JF001015

Ryan, J. C., Smith, L. C., van As, D., Cooley, S. W., Cooper, M. G., Pitcher, L. H., & Hubbard, A. (2019). Greenland ice sheet surface melt amplified by snowline migration and bare ice exposure. *Science Advances*, *5*(3), eaav3738. https://doi.org/10.1126/sciadv.aav3738

Saito, J., Meierbachtol, T., & Harper, J. (2023). Multi-decadal elevation changes of the land terminating sector of west greenland. *Journal of Glaciology*, *69*(273), 120–128. https://doi.org/10.1017/jog.2022.47

Scambos, T., Stroeve, J., & Koenig, L. (2013). *An intense greenland melt season: 2012 in review*. http://nsidc.org/greenland-today/2013/02/greenland-melting-2012-in-review/

Sellevold, R., van Kampenhout, L., Lenaerts, J. T. M., Noël, B., Lipscomb, W. H., & Vizcaino, M. (2019). Surface mass balance downscaling through elevation classes in an earth system model: Application to the greenland ice sheet. *The Cryosphere*, *13*(12), 3193–3208. https://doi.org/10.5194/tc-13-3193-2019

Slater, T., Hogg, A. E., & Mottram, R. (2020). Ice-sheet losses track high-end sea-level rise projections. *Nature Climate Change*, *10*, 879–881. https://doi.org/10.1038/s41558-020-0893-y

Slater, T., Shepherd, A., McMillan, M., Leeson, A., Gilbert, L., Muir, A., Munneke, P. K., Noël, B., Fettweis, X., van den Broeke, M., & Briggs, K. a. (2021). Increased variability in greenland ice sheet runoff from satellite observations. *PubMed*, *12*, 6069. https://pubmed.ncbi.nlm.nih.gov/34725324/

Smeets, P. C. J. P., van den Broeke, M. R., Boot, W., Cover, G., Eijkelboom, M., Greuell, W., Tijm-Reijmer, C. H., Snellen, H., & van de Wal, R. S. W. (2022). Automatic weather station data collected from 2003 to 2021 at the Greenland ice sheet along the K-transect, West-Greenland. https://doi.org/10.1594/PANGAEA.947483

Trusel, L. D., Das, S. B., Osman, M. B., Evans, M. J., Smith, B. E., Fettweis, X., McConnell, J. R., Noël, B. P. Y., & van den Broeke, M. R. (2018). Nonlinear rise in greenland runoff in response to post-industrial arctic warming. *Nature*, *564*, 104. https://doi.org/10.1038/s41586-018-0752-4

van de Wal, R. S. W., Boot, W., Smeets, P. C. J. P., Snellen, H., van den Broeke, M. R., & Oerlemans, J. (2012). Twenty-one years of mass balance observations along the k-transect, west-greenland. [Supplement to: van de Wal, RSW et al. (2012)]. *Earth System Science Data*, *4*, 31–35. https://doi.org/https://doi.org/10.1594/PANGAEA.779181

van As, D., Mikkelsen, A. B., Nielsen, M. H., Box, J. E., Liljedahl, L. C., Lindbäck, K., Pitcher, L., & Hasholt, B. (2017). Hypsometric amplification and routing moderation of greenland ice sheet meltwater release. *EGU The Cryosphere*, *11*, 1371–1386. https://tc.copernicus.org/articles/11/1371/2017/tc-11-1371-2017.pdf

van Kampenhout, L., Lenaerts, J. T. M., Lipscomb, W. H., Sacks, W. J., Lawrence, D. M., Slater, A. G., & van den Broeke, M. R. (2017). Improving the representation of polar snow and firn in the community earth system model. *Journal of Advances in Modeling Earth Systems*, *9*(7), 2583–2600. https://doi.org/https://doi.org/10.1002/2017MS000988

Vizcaino, M. (2014). Ice sheets as interactive components of earth system models: Progress and challenges. *WIREs Climate Change*, *5*(4), 557–568. https://doi.org/https://doi.org/10.1002/wcc.285

Vizcaino, M., Mikolajewicz, U., Ziemen, F., Rodehacke, C. B., Greve, R., & van den Broeke, M. R. (2015). Coupled simulations of greenland ice sheet and climate change up to a.d. 2300. *Geophysical Research Letters*, *42*(10), 3927–3935. https://doi.org/https://doi.org/10.1002/2014GL061142

Wang, S., Chen, J., Wilson, C., Li, J., & Hu, X. (2017). Reconciling grace and gps estimates of long-term load deformation in southern greenland. *Geophysical Journal International*, *212*, 1302–1313. https://doi.org/10.1093/gji/ggx473

Willeit, M., & Ganopolski, A. (2018). The importance of snow albedo for ice sheet evolution over the last glacial cycle. *Climate of the Past*, *14*(5), 697–707. https://doi.org/10.5194/cp-14-697-2018

Williams, J. J., Gourmelen, N., & Nienow, P. (2020). Dynamic response of the greenland ice sheet to recent cooling. *Scientific Reports*, *10*, 1647. https://doi.org/10.1038/s41598-020-58355-2

Zhou, T., Zhang, W., Chen, D., Zhang, X., Li, C., Zuo, M., & Chen, X. (2022). Understanding and building upon pioneering work of nobel prize in physics 2021 laureates syukuro manabe and klaus hasselmann: From greenhouse effect to earth system science and beyond. *Science China Earth Sciences*, *65*, 589–600. https://link.springer.com/content/pdf/10.1007/s11430-022-9906-4.pdf

A

Appendix

A.1. Figures

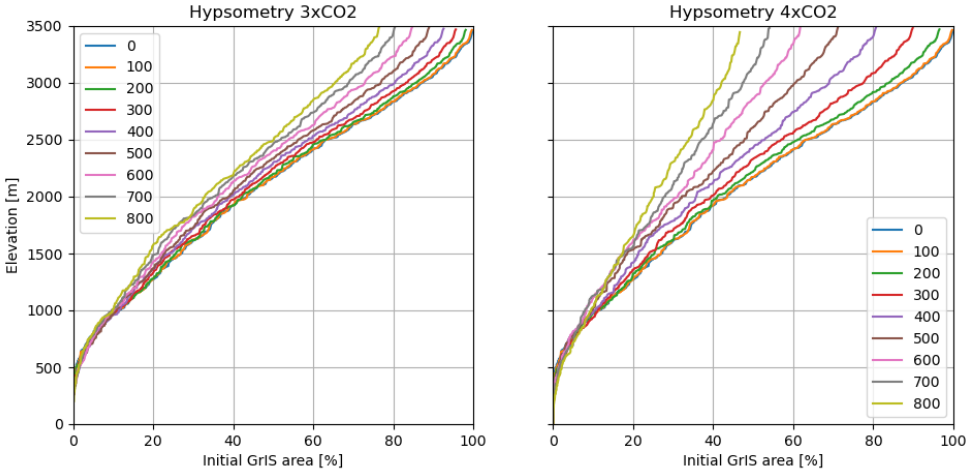

Figure A.1: Hypsometric curves through time

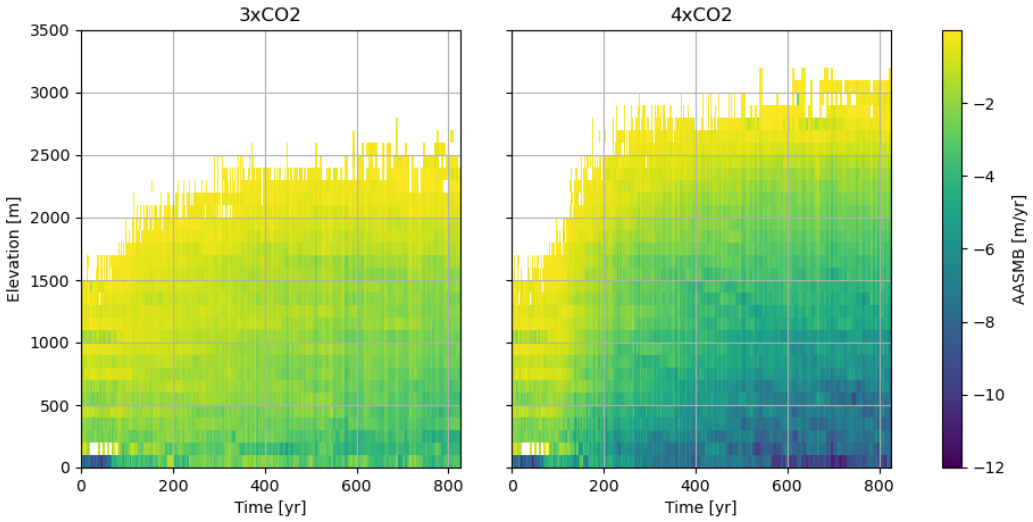

Figure A.2: Area-normalized SMB as a function of elevation and time

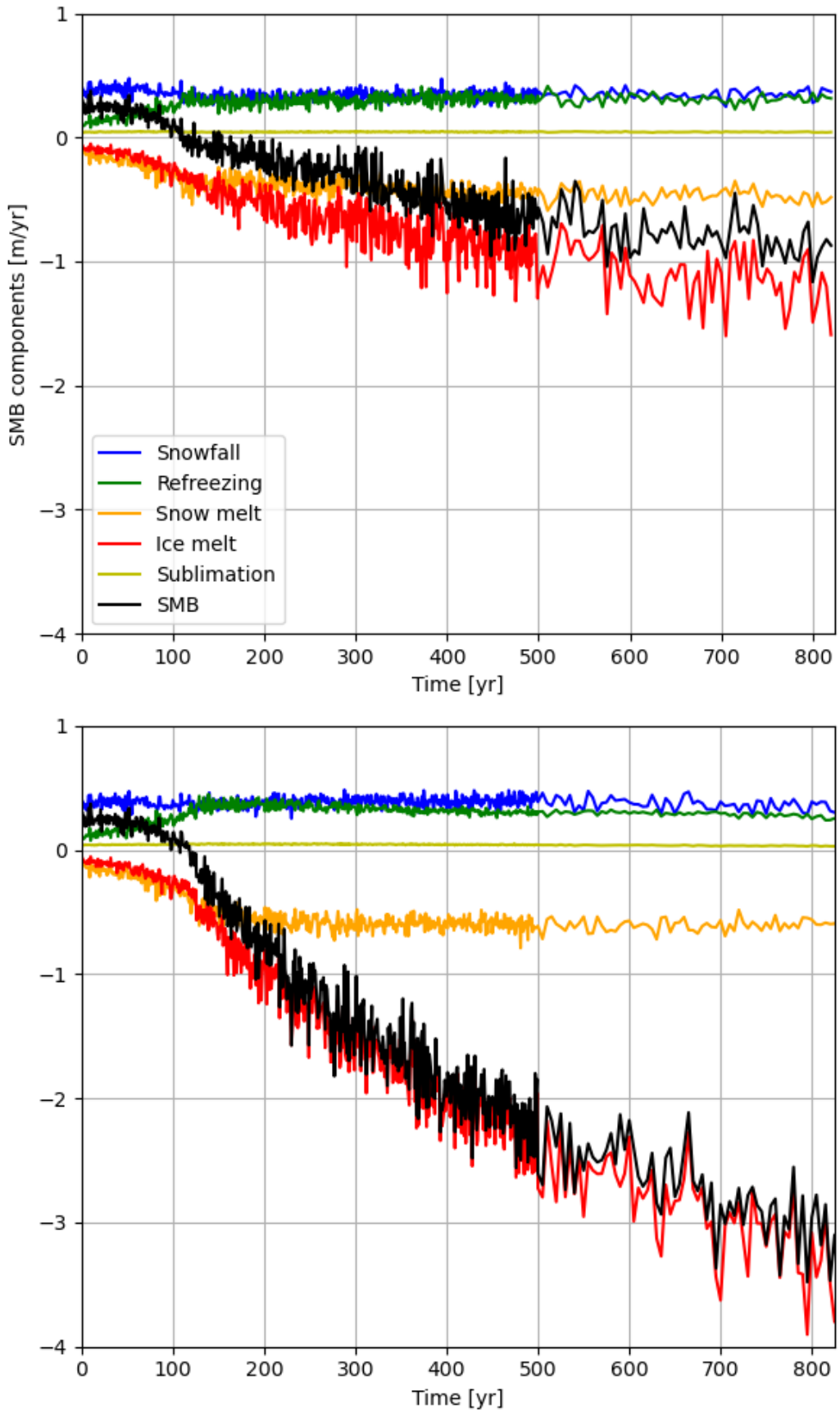

Figure A.3: Area-normalized SMB timeseries. $3xCO_2$ ($4xCO_2$) at the top (bottom).

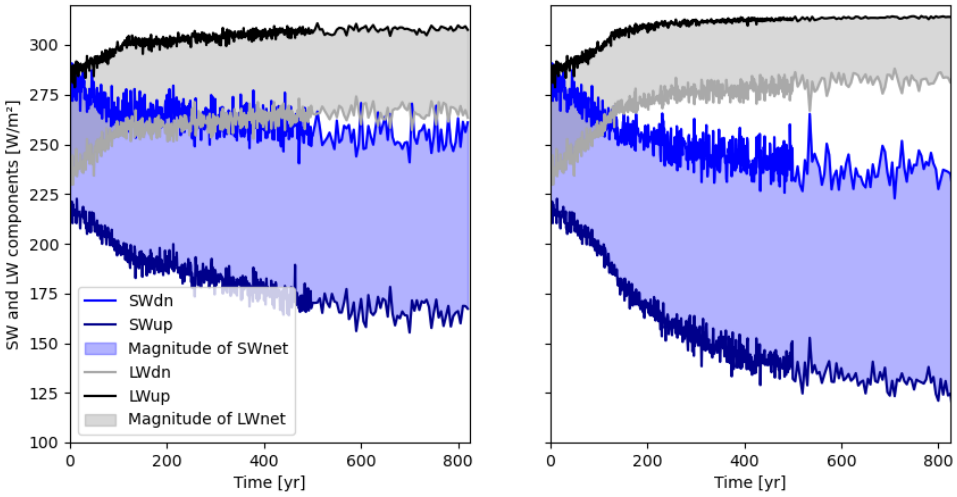

Figure A.4: Components for the SW and LW for 3xCO_2 (4xCO_2) on the left (right)

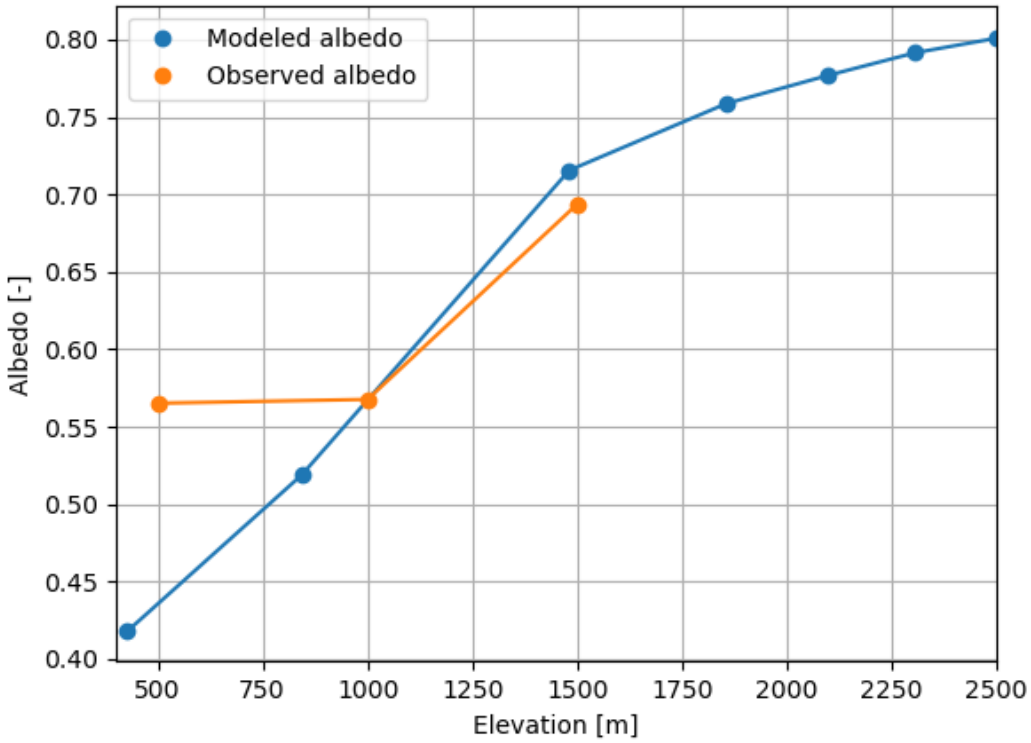

Figure A.5: Plot of albedo at the K-transect as a function of elevation (for years 2003-2013). Observation data are from Smeets et al., 2022, the model data is a historical-withism from Danabasoglu, 2019; Muntjewerf, Sellevold, et al., 2020.

Years	0-100	100-200	200-300	300-400	400-500	500-600	600-700	700-800
ELA	1030	1600	1810	1955	2071	2101	2161	2169
0-500	0.5	0.0	0.0	0.0	0.0	0.0	0.0	0.0
500-1000	17.3	1.4	0.3	0.1	0.0	0.0	0.0	0.0
1000-1500	40.0	6.6	1.9	0.6	0.1	0.1	0.0	0.0
1500-2000	102.3	42.3	21.3	13.2	7.3	5.8	1.9	1.8
2000-2500	165.7	126.5	115.2	92.0	71.8	66.1	48.5	51.3
2500-3000	186.9	160.8	156.8	155.8	140.6	136.9	112.8	105.2
3000-3500	69.6	67.0	67.4	70.3	69.9	73.0	69.2	68.6
Total	582.3	404.7	362.9	332.2	289.8	282.0	232.4	226.9

Table A.1: Century-averaged SMB values in Gt/yr in the accumulation area ($3xCO_2$)

Years	0-100	100-200	200-300	300-400	400-500	500-600	600-700	700-800
ELA	1030	1840	2339	2551	2673	2742	2779	2852
0-500	0.5	0.0	0.0	0.0	0.0	0.0	0.0	0.0
500-1000	17.3	0.6	0.0	0.0	0.0	0.0	0.0	0.0
1000-1500	40.0	4.2	0.0	0.0	0.0	0.0	0.0	0.0
1500-2000	102.3	28.5	1.6	0.2	0.0	0.0	0.0	0.0
2000-2500	165.7	107.5	33.2	6.9	0.3	0.0	0.0	0.0
2500-3000	186.9	180.1	131.5	82.0	46.3	29.3	19.8	10.4
3000-3500	69.6	77.2	85.0	85.6	80.2	66.6	46.2	31.2
Total	582.3	398.1	251.2	174.6	126.7	95.9	66.0	41.6

Table A.2: 100-year averaged SMB values in Gt/yr in the accumulation area ($4xCO_2$)

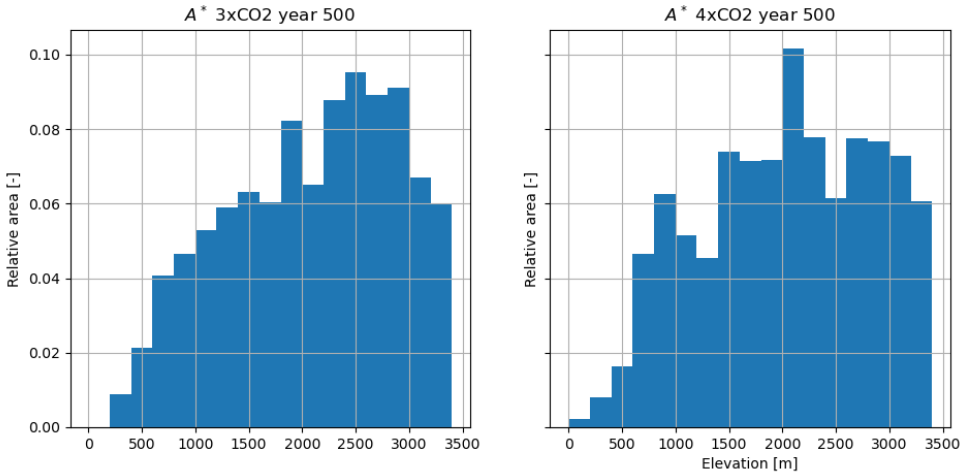

Figure A.6: Area distribution A* as a function of elevation (the derivative of the hypsometry)

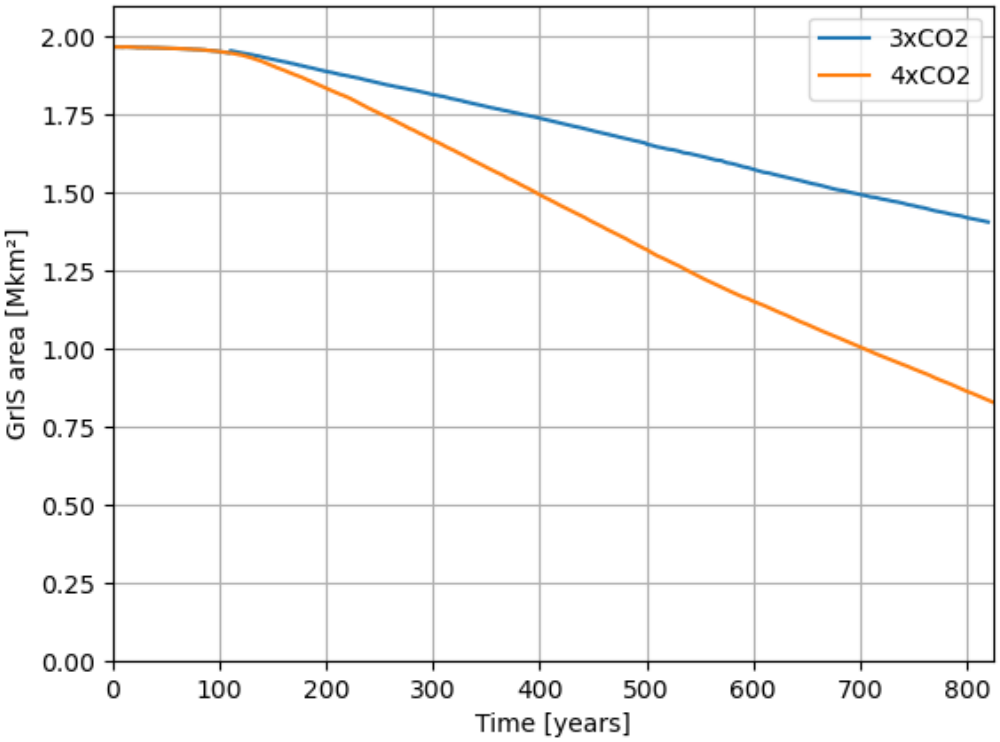

Figure A.7: Time series of the GrIS area for both scenarios

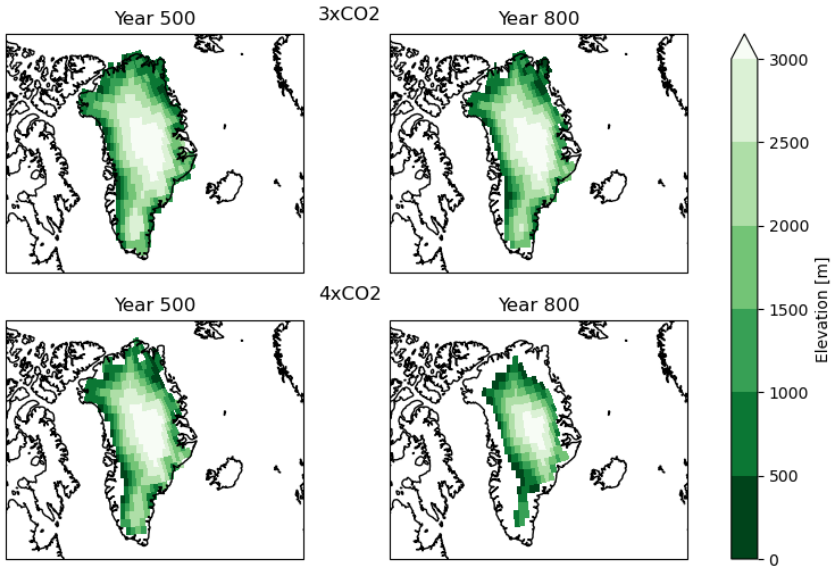

Figure A.8: Elevations maps for both scenarios for years 500 and 800

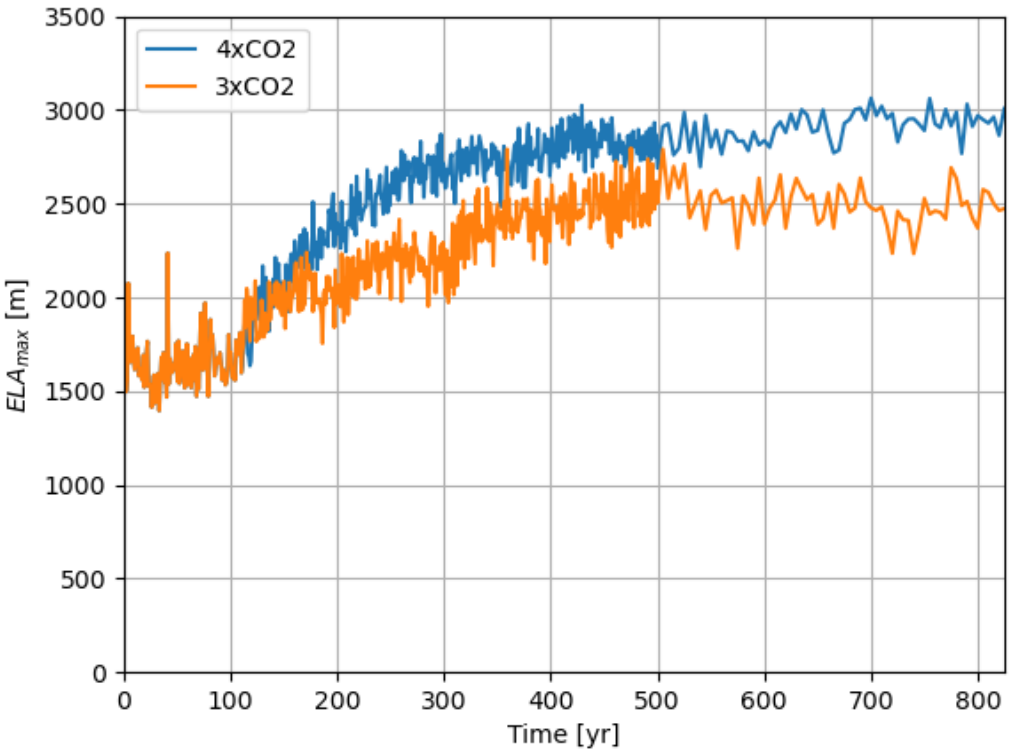

Figure A.9: Timeseries of $\mathrm{ELA}_{\mathrm{max}}(t)$ for both $3\mathrm{xCO}_2$ and $4\mathrm{xCO}_2$

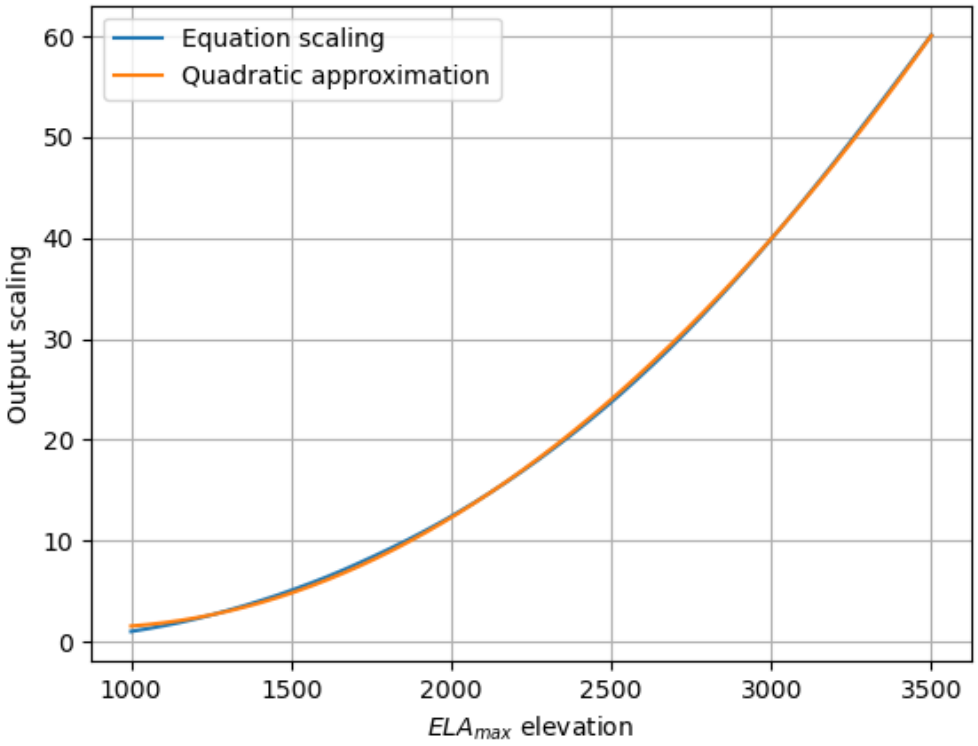

Figure A.10: Scaling of the ELA_{max}

B

Maps

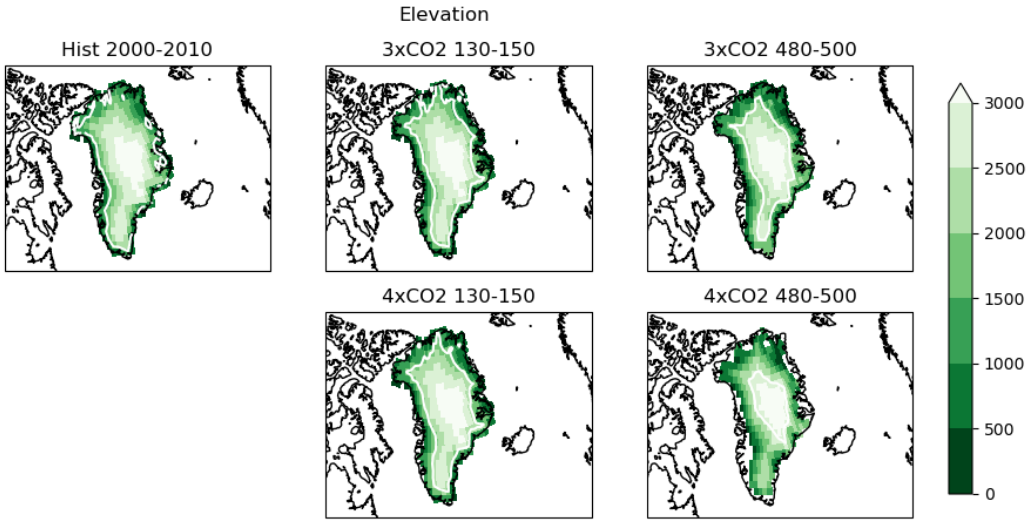

Figure B.1: Maps of the elevation for historical (top left), 3xCO_2 (top) and 4xCO_2 (bottom) scenarios. Top left represents elevation averaged over years 2000-2010 CE, the centre are for 130-150, and the right are for 480-500. The white contour line is the equilibrium line altitude.

B.1. Maps of annual SMB, melt and refreezing

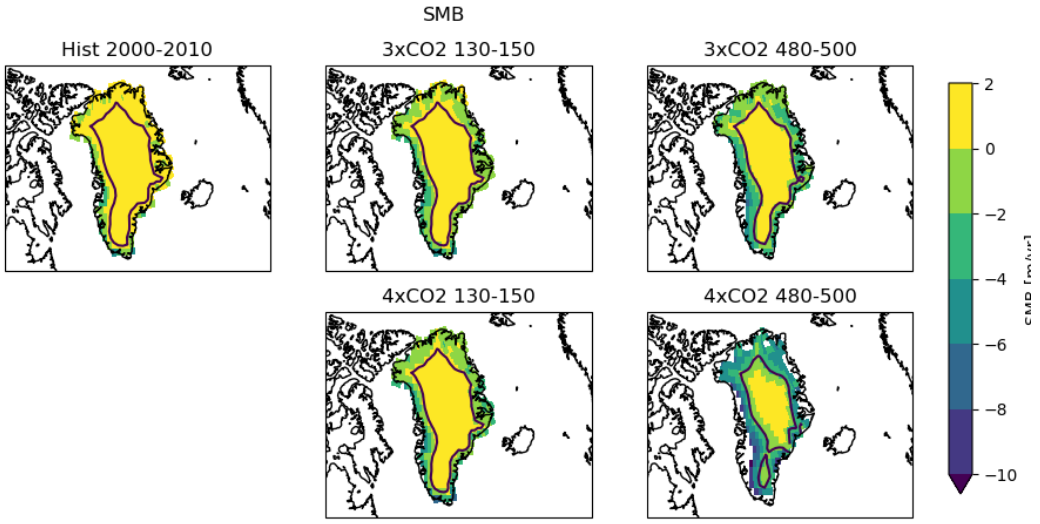

Figure B.2: Maps of the annual SMB for historical (top left), 3xCO_2 (top) and 4xCO_2 (bottom) scenarios. Top left represents SMB averaged over years 2000-2010 CE, the centre are for 130-150, and the right are for 480-500. The black line is the 2000 m elevation contour line.

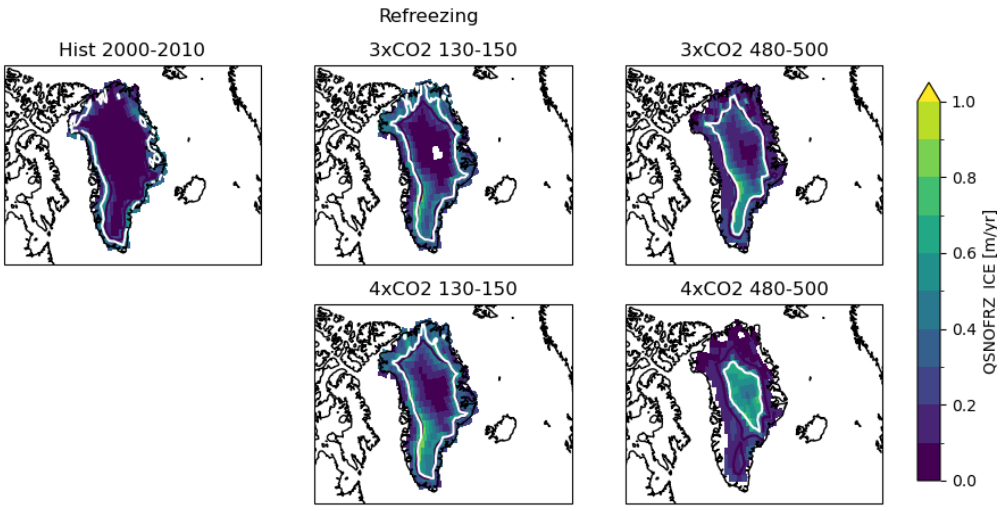

Figure B.3: Maps of the annual refreezing for historical (left), 3xCO_2 (centre) and 4xCO_2 (right) scenarios. Top left represents refreezing averaged over years 2000-2010 CE, the other in the top row are for 130-150, and the bottom row for 480-500. The black line is the 2000 m elevation contour line, and the white contour shows the ELA.

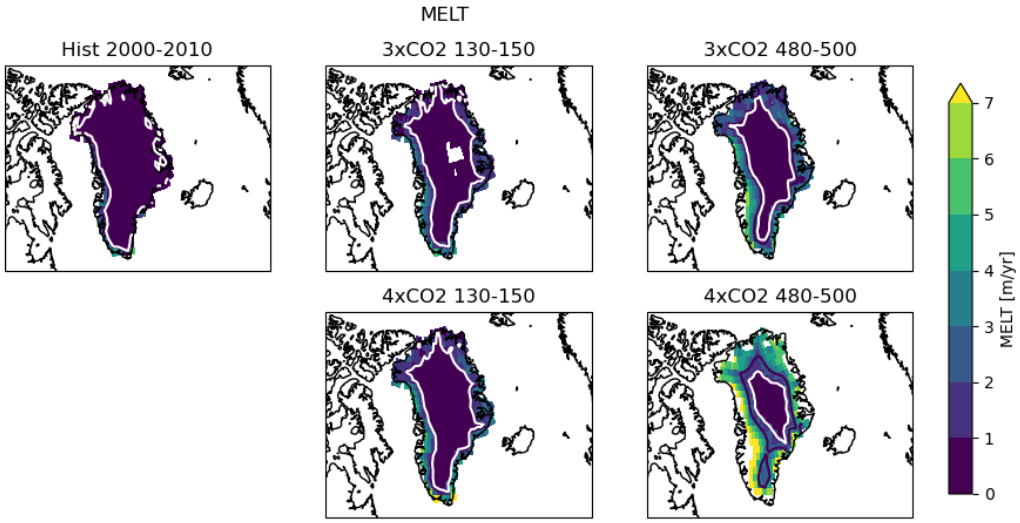

Figure B.4: Maps of the annual melt (snow melt and ice melt combined) for historical (left), 3xCO_2 (centre) and 4xCO_2 (right) scenarios. Top left represents refreezing averaged over years 2000-2010 CE, the other in the top row are for 130-150, and the bottom row for 480-500. The black line is the 2000 m elevation contour line, and the white contour shows the ELA.

B.2. Maps of summer SEB

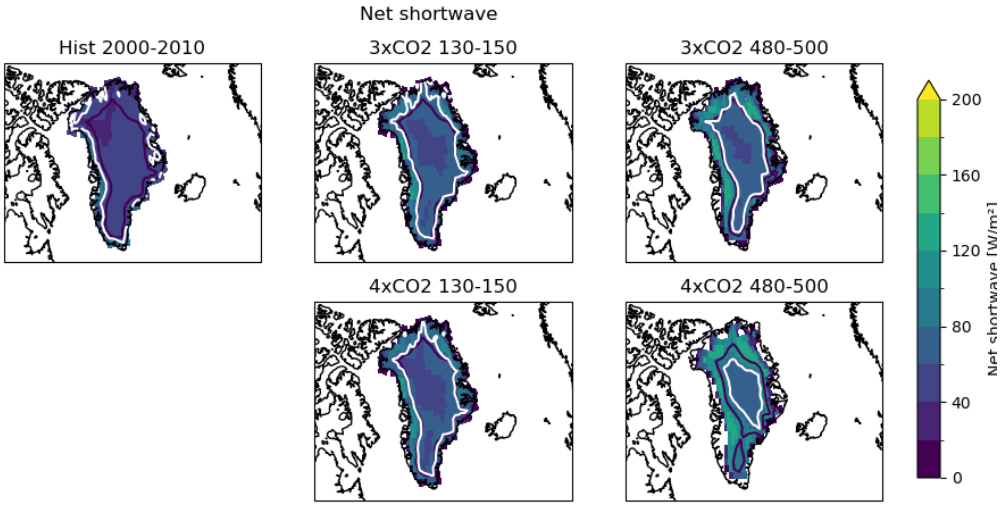

Figure B.5: Maps of average JJA net SW. Positive heats the ice sheet. The black line is the 2000 m elevation contour line, and the white contour shows the ELA.

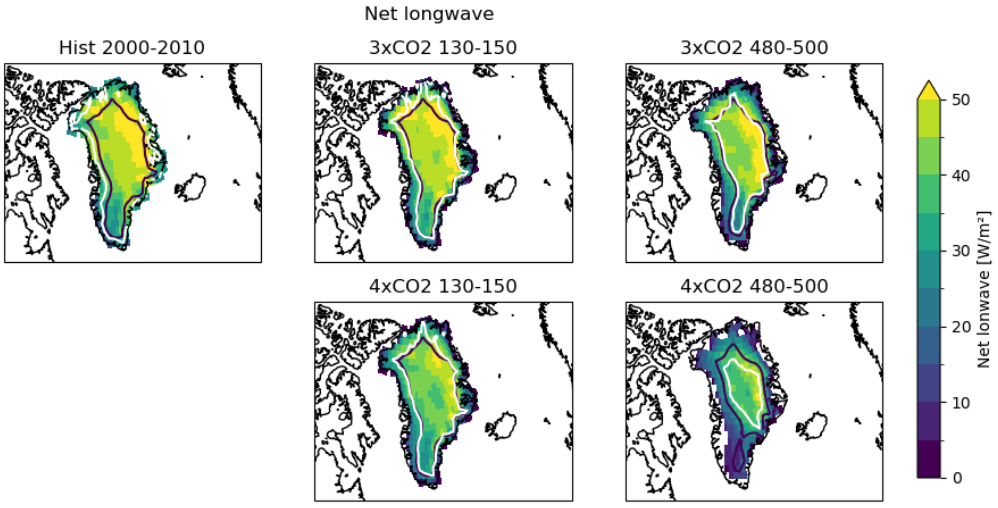

Figure B.6: Maps of average JJA net LW. Positive heats the ice sheet. The black line is the 2000 m elevation contour line, and the white contour shows the ELA.

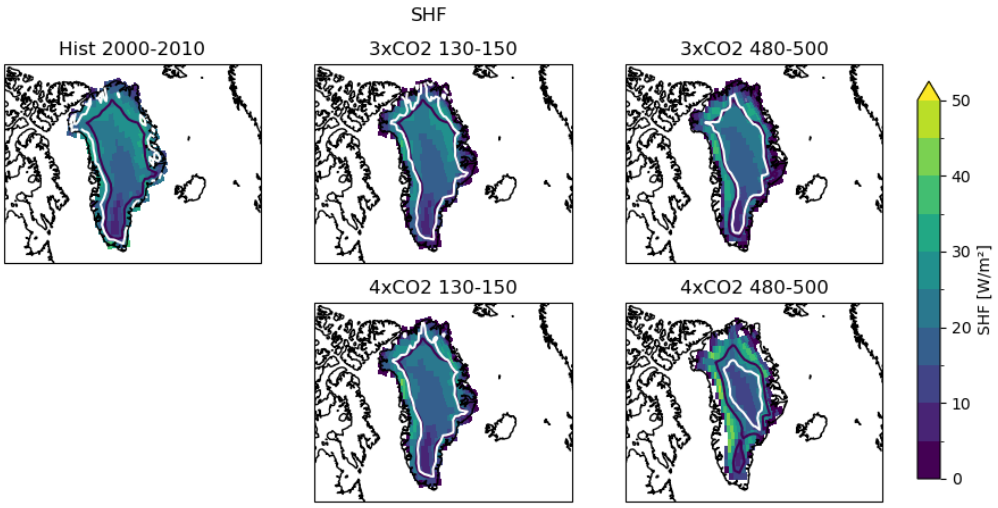

Figure B.7: Maps of average JJA SHF. Positive heats the ice sheet. The black line is the 2000 m elevation contour line, and the white contour shows the ELA.

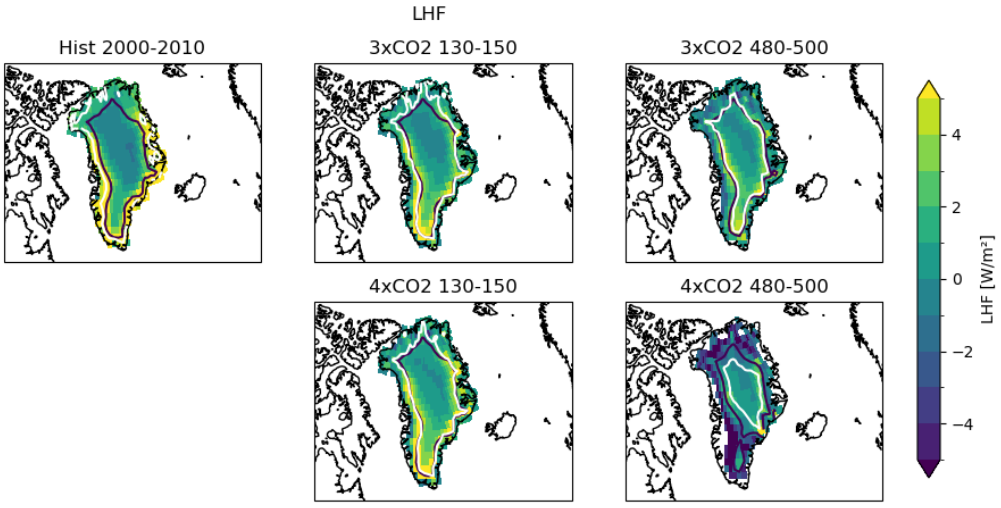

Figure B.8: Maps of average JJA LHF. Positive heats the ice sheet. The black line is the 2000 m elevation contour line, and the white contour shows the ELA.